J. Fluid Mech. (1996), *vol.* 311, *pp.* 37–71

Copyright © 1996 Cambridge University Press

Transitions to chaos in a forced jet: intermittency, tangent bifurcations and hysteresis

By GEORGE BROZE AND FAZLE HUSSAIN
Department of Mechanical Engineering, University of Houston, Houston, TX 77204-4792, USA

(Received 5 September 1994 and in revised form 18 October 1995)

Experimental studies of a forced transitional jet at moderate Reynolds numbers reveal interesting transitions between low-dimensional states, namely tangent bifurcations, intermittency and hysteresis. The experiments were carried out in an axisymmetric air jet with a laminar top-hat exit profile in the low-noise ambient of a large anechoic chamber, using forcing amplitude and frequency as control parameters. Tangent bifurcations are seen to occur in two different transitions from periodicity to chaos: (i) from stable pairing to nearly periodic modulations of pairing and (ii) from stable double pairing to a quarter-harmonic chaotic attractor. In case (i), an empirically derived mapping closely reproduces the temporal dynamics of one chaotic attractor at a point just after the tangent bifurcation. In case (ii), the intermittency was characterized by estimating the scaling exponent of the p.d.f. of the periodic durations, which was found to be close to the characteristic value for type-II intermittency. Hysteresis is seen at higher Strouhal numbers in the transitions between aperiodic modulations and the periodic/chaotic double pairing states. Based on simultaneous flow visualization and velocimetry, the hysteresis appears to be associated with intermittent tilting of (otherwise) axisymmetric vortices. These transitions are explained in terms of feedback-driven dynamics from vortex roll-ups and pairings, which can be phase-locked (periodic) or unlocked (nearly quasi-periodic and chaotic). The observed transitions connect large regions of deterministic behaviour in the phase diagram, confirming the existence of a low-dimensional dynamical system in transitional jets – an open flow of technological relevance.

Two-point coherence measurements indicate that spatial coupling (and, hence, coherent motion from pairing dynamics) extends for five to eight diameters from the exit, well beyond the locations of pairing and double pairing. This justifies the use of single-point measurements and confirms our hypothesis that the dynamics in this convectively unstable flow are primarily temporal rather than spatio-temporal.

1. Introduction

The prospect of describing flows as low-dimensional dynamical systems implies that substantially fewer degrees of freedom (than in numerical simulations) may be adequate to model and control flow transition, and perhaps even turbulence. In order to achieve these goals, it is first necessary to develop a *conceptual* model of the dynamics and identify relevant control parameters, dynamical states and transitions between states. The existence of a low-dimensional dynamical system in an *open* flow (typical of most technological applications) was hypothesized and experimentally verified by Broze & Hussain (1994, hereinafter referred to as BH), who presented a phase diagram and evidence of two periodic and two chaotic attractors in circular jets.

In this paper, we explore the transitions between these states in order to substantiate the proposed conceptual dynamical system. Further, we provide interpretations of these states and transitions in terms of the dominant vortex dynamics in the jet transition region. These results are intended to lay a foundation for and provide validation of future quantitative models and control approaches.

The application of dynamical systems techniques in open free-shear flows presents an even greater challenge than in closed flows, since open flows are typically *convectively unstable* and hence very susceptible to ambient noise. (Note that open flows are encountered in most situations in nature and technology but have been least studied as dynamical systems because of their inherent complexity.) For convectively unstable flows (such as jets) to have dominant low-dimensional dynamics, they require feedback from downstream events to initiate upstream instabilities (which will otherwise be triggered by 'high-dimensional' noise, inherent in a practical environment). To emphasize this noise susceptibility, definitions were proposed in BH to distinguish between flows which are 'physically' open (with mass flux across the control volume boundaries) and 'dynamically' open (i.e. noise driven). The argument put forth there was that low-dimensional dynamics in a noise-susceptible (open) flow implies self-excitation (via feedback) and hence dynamical closure. Hereafter in this paper (with the exception of discussion in §5), we use 'open' only to refer to flow geometry but not necessarily dynamics.

Transitions from order to chaos (and hence, presumably, to turbulence) in flow systems have been studied in the past using both stability and dynamical systems theory. Four routes to chaos are frequently observed in dynamical systems models: (i) a quasi-periodic route via a sequence of Hopf bifurcations (Ruelle & Takens 1971; Newhouse, Ruelle & Takens 1978), (ii) an infinite sequence of period-doubling bifurcations leading to chaos (Grossmann & Thomae 1977; Feigenbaum 1978; Coullet & Tresser 1978), (iii) a direct transition to chaos via intermittency (Pomeau & Manneville 1980), and (iv) a homoclinic catastrophe (see Guckenheimer & Holmes 1983, §6.5). These routes have been observed in closed flow experiments (quasi-periodic route: Taylor–Couette flow – Brandstäter & Swinney 1987; Rayleigh–Bénard convection – Jensen *et al.* 1985; period doubling: Rayleigh–Bénard convection – Libchaber & Maurer 1980; intermittency: Rayleigh–Bénard convection – Bergé *et al.* 1980; Dubois, Rubio & Bergé 1983; homoclinic chaos – Mullin & Price 1989). In open flows, some examples of apparent chaos have been found, but only a few definitive results have been reported about the transitions to chaos. Sreenivasan (1985) observed a quasi-periodic route to chaos in a cylinder wake with aeroelastic coupling; Van Atta & Gharib (1987) argued against the possibility of such a scenario occurring in a uncoupled wake. Williams-Stuber & Gharib (1990) found a quasi-periodic route to chaos in an aerofoil wake, using two forcing frequencies in addition to the natural shedding frequency (thus directly controlling almost all facets of the dynamics). We know of no prior experimental evidence of tangent bifurcations or intermittency routes to chaos in open flows.

Another important phenomenon is hysteresis near transition points, associated with subcritical bifurcations. Hysteresis has the profound implication that flow states are non-unique for a given set of control parameter values and instead depend on the path in parameter space (and hence the initial condition); hysteresis has been observed in a limited number of open flow experiments. Muylaert (1980) found hysteresis in the pressure coefficient c_p as the angle of attack α of a delta wing was varied, with jumps in c_p presumably corresponding to the appearance and disappearance of vortex breakdown. In experiments similar to Muylaert's, Gersten *et al.* (1985) noted that this

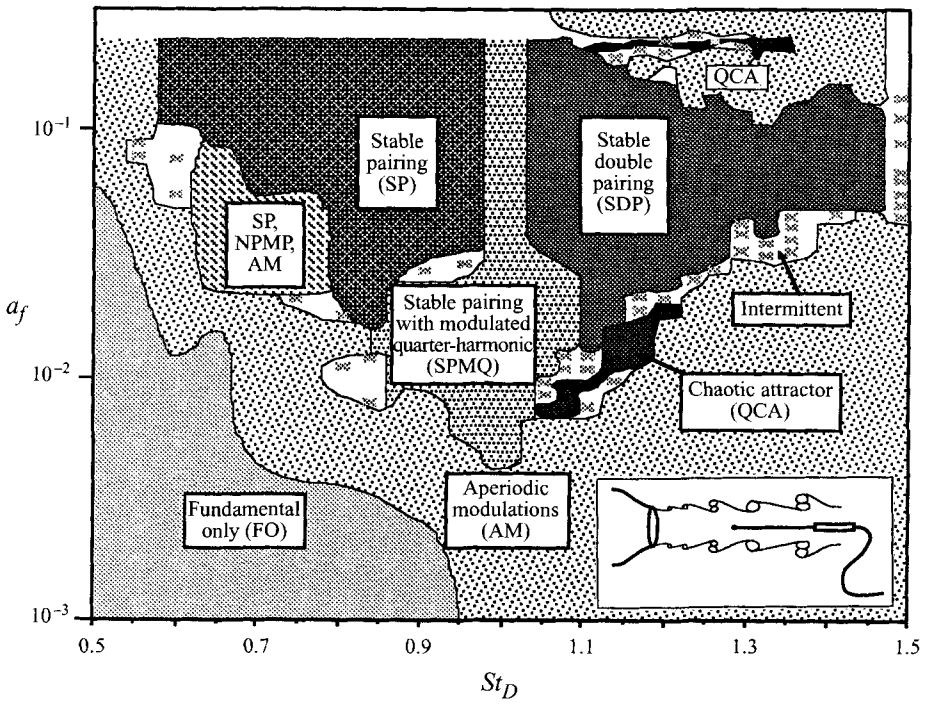

FIGURE 1. Phase diagram of the transitional circular jet in the St_D, a_f parameter space. The inset shows a schematic of the nozzle, vortex dynamics and probe location.

hysteresis was a function of Mach number M and conjectured that it would appear as a cusp singularity near $M \approx 0.5$. They showed the onset and growth of the hysteresis region in the (c_p, α)-plane as the spanwise air-blowing coefficients c_Q was varied. Spotar & Terekhov (1987) found apparently bistable flow patterns in turbulent swirling jets impinging on a plane, which was discussed theoretically by Shtern & Hussain (1993). The flow alternated between the two states on slow time scales, suggesting intermittency but also consistent with a hysteretic system near a cusp with jumps caused by finite-amplitude disturbances.

BH presented an experimentally determined phase diagram (repeated here as figure 1 for convenience) and evidence of periodic and chaotic attractors related to the vortex dynamics of the transition region of a forced circular jet using two control parameters: non-dimensional forcing amplitude a_f ($\equiv u_f'/U_e$) and frequency St_D ($\equiv f_{ex} D/U_e$) – where D is the jet diameter, U_e is the jet exit mean velocity, f_{ex} is frequency of excitation and u_f' is the r.m.s. longitudinal velocity fluctuation at the jet exit. As discussed in Appendix A, Reynolds number Re_D ($\equiv DU_e/\nu$, where ν is the kinematic viscosity) has little effect on the dynamics at the high Re_D used here; its effects are considered briefly in §3.2. A brief description of each state is given in table 1. In this paper we present experimental evidence of transitions between these states (namely tangent bifurcations, intermittency and hysteresis) and interpret them in terms of vortex dynamics. The paper is organized as follows. Section 2 provides evidence of tangent bifurcations in two different transitions in the jet flow. In §3, we present data from the hysteresis region in the parameter space and an idealized picture of the local bifurcation surface. To confirm that the dynamical system is indeed temporal, we present coherence measurements in §4 to indicate the strength and spatial extent of dynamical coupling.

Acronym	Name	Dynamics
SP	Stable pairing	Single vortex pairings are periodic in time and their pairing location is fixed in space
NPMP	Nearly periodic modulations of pairing	Pairings are chaotic (nearly quasi-periodic) in time; pairing location oscillates up- and downstream
SDP	Stable double pairing	First and second pairings are periodic in time and fixed in space
QCA	Quarter-harmonic chaotic attractor	Overall sequence of vortex dynamics is chaotic in time; first and second pairing locations oscillate up- and downstream
INT	Intermittency	Switches non-periodically between two states (notably SDP and QCA)
AM	Aperiodic modulations	Non-periodic in time; apparent switching between axisymmetric and titled vortices (see at higher St_D)
SPMQ	Stable pairing with modulated quarter-harmonic	First pairing is apparently periodic in time, but second pairing is weakly modulated
FO	Fundamental only	Non-periodic in time with no apparent pairings; a sharp spectral peak at the forcing frequency sits on a broadband pedestal

TABLE 1. Summary of flow states shown in the phase diagram (figure 1).

In the concluding remarks (§5), we briefly discuss the implications of these results for vortex interactions in the jet.

2. Tangent bifurcations and intermittency

Of the known routes to chaos, the one found in our experiments is intermittency via a tangent bifurcation. There are two transitions which demonstrate this clearly: (i) from SP to NPMP and (ii) from SDP to QCA. These four states and their dynamical invariants are documented in BH; their locations in the (St_D, a_f) parameter space are shown in figure 1. As indicated in table 1, SP and SDP are periodic attractors, and QCA and NPMP are chaotic attractors. These transitions are discussed in §§2.1 and 2.2.

2.1. *SP–NPMP transition*

NPMP is seen in two narrow parameter bands: $0.65 \leqslant St_D \leqslant 0.73$, $a_f \approx 3$–4% and $a_f \approx 7$–8% (see figure 7 in BH). NPMP always has SP as a neighbour in parameter space and is quite likely to be the result of a bifurcation from this periodic state; this transition is illustrated by three traces shown in figure 2 at $St_D \approx 0.68$ (the time axis indicates the portion of figure 3 to which figure 2 corresponds). Periodic constant-amplitude SP is seen in the first trace for $a_f \approx 4.3\%$. At $a_f \approx 3.7\%$, trace (ii) shows intermittent modulated pairing and SP. Finally, by (iii) $a_f \approx 3.4\%$, the segments of SP are gone, and the modulated pairing has become nearly periodic (hence NPMP).

In order to analyse this transition further, the signals were decomposed into the modal amplitudes and phases using the procedure described in Appendix B. Vortex roll-up and pairing are the dominant events in the jet near field, and subharmonic resonance is the mechanism of vortex pairing which is crucially dependent on the modal amplitudes and phase difference (Monkewitz 1988); however, being forced at a constant level, fundamental amplitude plays the role of a parameter rather than a dynamical variable. Thus, the subharmonic amplitude a_s and the fundamental–subharmonic phase difference ϕ_s are the dynamical variables of the system. Data

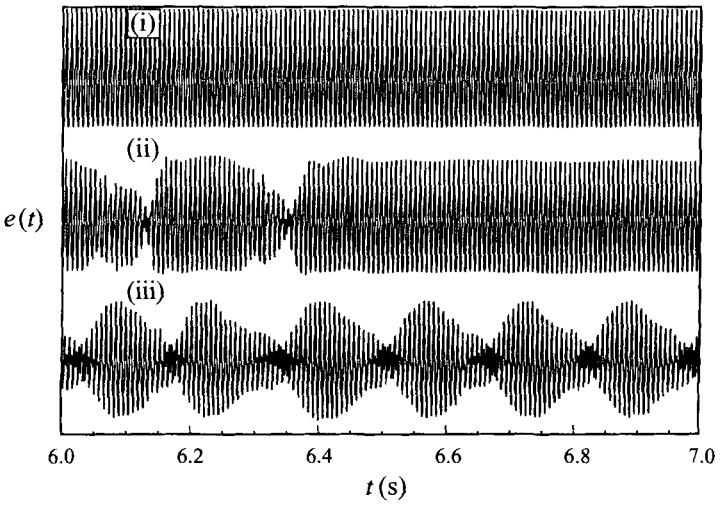

FIGURE 2. Time traces of the transition from stable pairing SP to near periodic modulations of pairing NPMP at $St_D \approx 0.68$, $Re_D \approx 4.0 \times 10^4$: (i) $a_f \approx 4.3\%$, (ii) $a_f \approx 3.7\%$, and (iii) $a_f \approx 3.4\%$. Hot wire located at $x/D = 1.5$ on the jet centreline.

were taken on the jet centreline at $x/D \approx 1.5$, a point downstream of vortex roll-up where the fundamental has saturated and subharmonic resonance (leading to vortex pairing) has begun. Although measurements anywhere within the potential core are, in principle, able to reveal the dynamics (see §4), a site between the saturation of the fundamental and subharmonic is particularly apt for capturing the pairing dynamics.

In figure 3, sequences of (*a*) a_s and (*b*) ϕ_s are shown at the same St_D and a_f as figure 2. The direct correspondence between the signal and a_s–ϕ_s time sequences can be seen by comparing figure 2 with the interval $6 \leqslant t \leqslant 7$ in figure 3. For $a_f \approx 4.3\%$, a_s is high and constant and ϕ_s is fixed, as is expected for SP. In the intermittent state at $a_f \approx 3.7\%$, modulated pairing is indicated by fall-off and rise of a_s and the corresponding jumps in ϕ_s; at other times, varying intervals of SP are indicated by fixed a_s and ϕ_s. Finally, for NPMP (case iii), a_s shows the expected nearly periodic variations, with a (positive) jump in ϕ_s at each a_s minimum. Thus this sequence for decreasing a_f indicates a transition from a periodic state (SP) to a nearly quasi-periodic, chaotic state (NPMP) via intermittency.

From the discrete sequences of a_s and ϕ_s in figure 3, return maps were constructed to reveal the transition dynamics. The return maps for SP are obviously fixed points for both a_s and ϕ_s, while those for the intermittent case are a mixture of those for SP and NPMP. Therefore, only maps for NPMP are shown. Figure 4(*a*) shows a plot of a_s versus ϕ_s; the subscript n refers to the number of the realization in the sequence. There is a peak near $\phi_s = 0.2\pi$ where points are densely clustered; this is the preferred phase angle, and a_s reaches a maximum here. This corresponds to the maxima of the envelope of the time trace shown in figure 2(iii). Around this ϕ_s value, a_s falls off sharply, reaching a minimum near $\phi_s = 0.7\pi$. The variation of a_s with ϕ_s is apparently π-periodic (as is expected). There is a discernible loop in the plot near the a_s maximum, implying that the function is multivalued, perhaps due to a projection from the actual higher-dimensional state space onto this two-dimensional one. This figure reveals both a preferred phase angle and the strong dependence of a_s on ϕ_s (especially near the a_s maximum), as expected from subharmonic resonance theory. Husain & Hussain (1989) measured subharmonic amplitude as a function of initial ϕ_s at a location upstream of

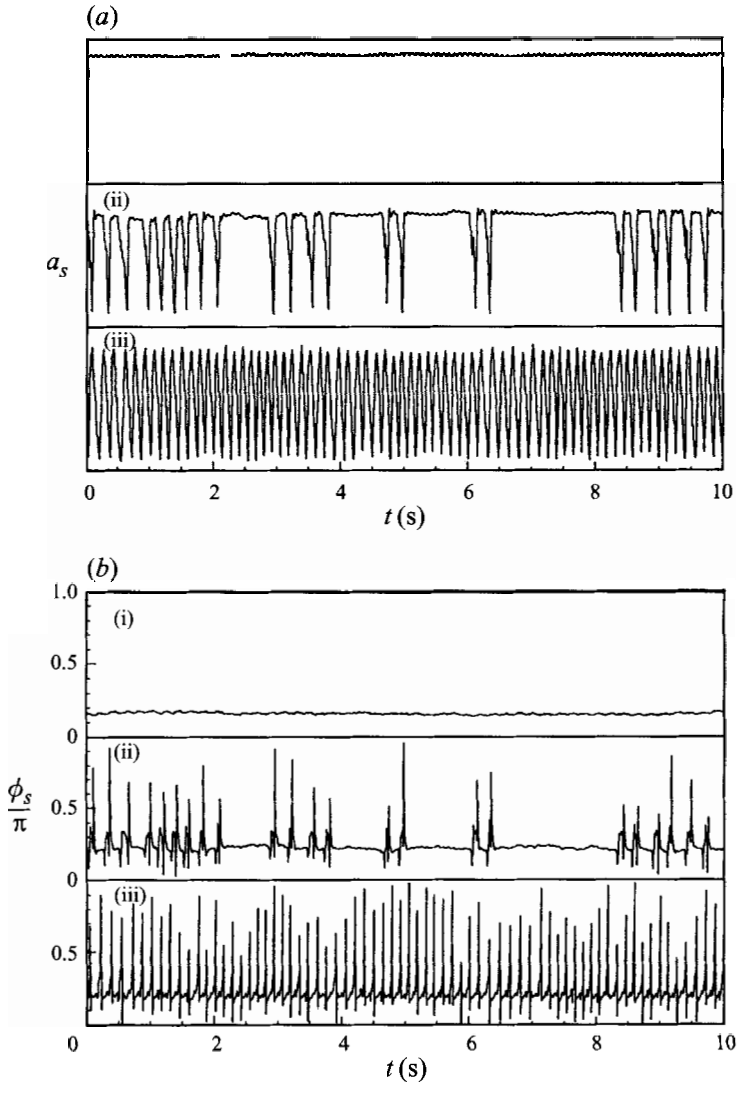

FIGURE 3. Time sequences of (*a*) the subharmonic amplitude a_s and (*b*) the fundamental–subharmonic phase difference ϕ_s in the transition from stable pairing SP to nearly periodic modulations of pairing NPMP at $St_D \approx 0.68$, $Re_D \approx 4.0 \times 10^4$, $x/D = 1.5$: (i) $a_f \approx 4.3\%$, (ii) $a_f \approx 3.7\%$, and (iii) $a_f \approx 3.4\%$.

subharmonic saturation in a single-stream axisymmetric mixing layer; in their experiments, however, they controlled the initial amplitudes of both components (a_{f0}, a_{s0}) and their initial phase difference (ϕ_{in}) at the separation point. Figure 3(*b*) in Husain & Hussain resembles an inverted image of figure 4(*a*) here, with a broad maximum and a cusp-like minimum. The difference between their figure and ours is because they plot local subharmonic amplitude versus *initial* phase difference; here we use the *local* phase difference. When resonance occurs, the local ϕ_s is fixed regardless of initial ϕ_s; hence, all high a_s at this location will occur at nearly the same ϕ_s.

The first-return map of a_s is shown in figure 4(*b*). The loop structure resembles either loop of the NPMP Poincaré section shown in BH. The details found in the Poincaré section (such as folds and accumulation points) are not seen here, because the amplitudes are integrals (i.e. averages) over short segments of the signal rather than

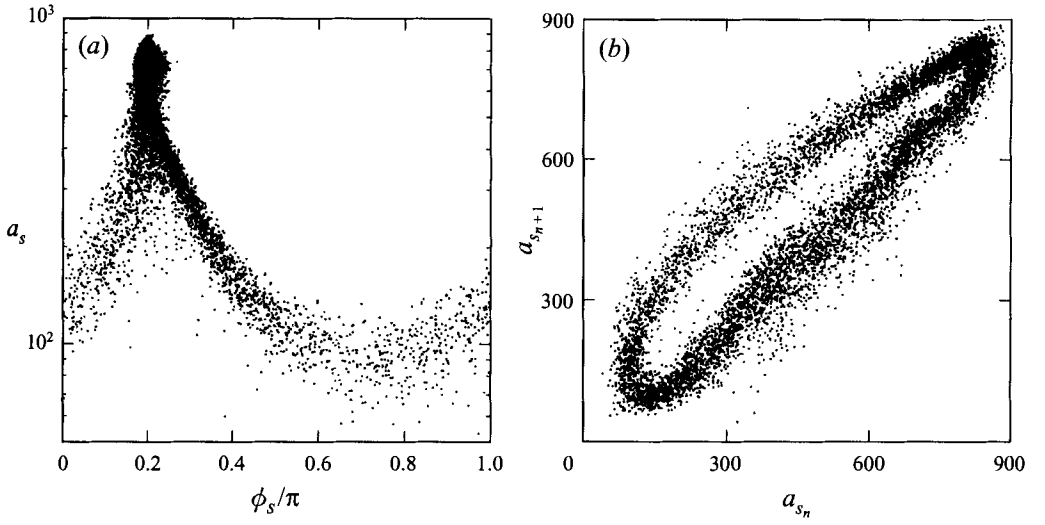

FIGURE 4. (*a*) Subharmonic amplitude a_s versus phase difference ϕ_s; (*b*) first-return map of a_s for nearly periodic modulations of pairing NPMP. $St_D \approx 0.68$, $a_f \approx 3.40\%$, $Re_D \approx 4.0 \times 10^4$, $x/D = 1.5$.

being instantaneous amplitudes (see Appendix B for details). Nevertheless, the basic cycle nature of the amplitude is revealed in this plot.

Figure 5(*a*) shows the first-return map of ϕ_s, which reveals some very interesting features of the transition from SP to NPMP. From the scattered points, one can infer an underlying curve, or 'map function', which enters on the left at $\phi_s/\pi \approx 0.15$, crosses or becomes tangent to the diagonal at $\phi_s/\pi \approx 0.2$, rises and wraps at the top from about (0.6, 1.0) to (0.6, 0), and then levels off and wraps at the right side from about (1.0, 0.15) to (0, 0.15). The phase wrapping occurs because a phase difference of 0 and π are the same: a shift of the subharmonic by π results in the same relative phase of the fundamental to the subharmonic. Before addressing this particular map, some general discussion about this type of map will be presented.

As mentioned above, the map function may (i) cross the diagonal or be (ii) tangent or (iii) nearly tangent to it. If the map function crosses the diagonal, there would be two intersections, resulting in one stable and one unstable fixed points of the dynamical system. (Crossings of the diagonal are fixed points because at these points $\phi_{n+1} = \phi_n$.) In this case, iterates would accumulate at the stable fixed point, and the system would remain in that state. This is the case in SP, where ϕ_s remains nearly constant in time when measured at a fixed location in space. (Although the flow is $2/f_{ex}$-periodic, ϕ_s is determined from integrals over a full subharmonic period and thus would have a constant value in the sequence.) In case (ii), the two fixed points meet at the point of tangency and become a single fixed point with marginal stability; this is a *tangent* bifurcation point in parameter space. In case (iii), the map function lies above the diagonal; the bifurcation has taken place and no fixed points of the map (period-1 periodic states of the flow) can exist. The post-bifurcation state can be one of several cases: (i) a periodic map of period n; (ii) a quasi-periodic map; or (iii) a chaotic map. A necessary condition for chaos in one-dimensional maps is that the map function be non-invertible.

In the light of this information, we will discuss figure 5(*a*). As was seen in figures 2 and 3, SP becomes NPMP by apparent intermittency. The NPMP ϕ_s return map seems (underlying the scatter) to reveal a tangent bifurcation, as is expected in an

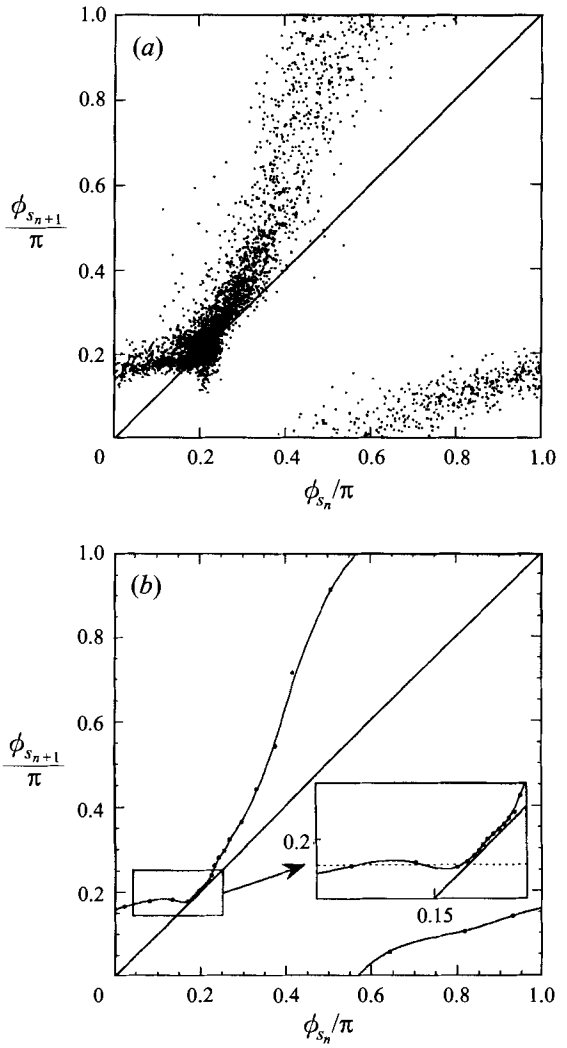

FIGURE 5. (*a*) First-return map of phase difference ϕ_s; (*b*) averaged first-return map of ϕ_s for nearly periodic modulations of pairing NPMP. Flow parameters the same as for figure 4.

intermittency transition. If this is true, then the points in the map should not fall on or below the diagonal, but this occurs near $\phi_s/\pi \approx 0.2$ (figure 5*a*). There are two possible explanations for this phenomenon: (i) the map is marginally stable and is being perturbed out of its fixed point by flow noise; or (ii) there is no fixed point, but flow and measurement noise contaminates the measurements of ϕ_s. Explanation (i) is not probable since the flow dynamics are so nearly quasi-periodic (and the map dynamics so nearly periodic); it is quite unlikely that (random) noise could perturb the map away from the fixed point as periodically as is the case in our experiments (see later discussion regarding figure 6). A case of regularly occurring noise-driven intermittency has been observed in perturbed homoclinic orbits in a flow model (Aubry *et al.* 1988), but there is no reason to believe a homoclinic connection exists here. Explanation (ii) is thus more feasible: estimates of ϕ_s are contaminated by flow noise. The noise is unavoidable; in order to make the measurements as 'instantaneous' as possible, the minimum possible size of signal segment was used, i.e. $\tau = 2/f_{ex}$. The

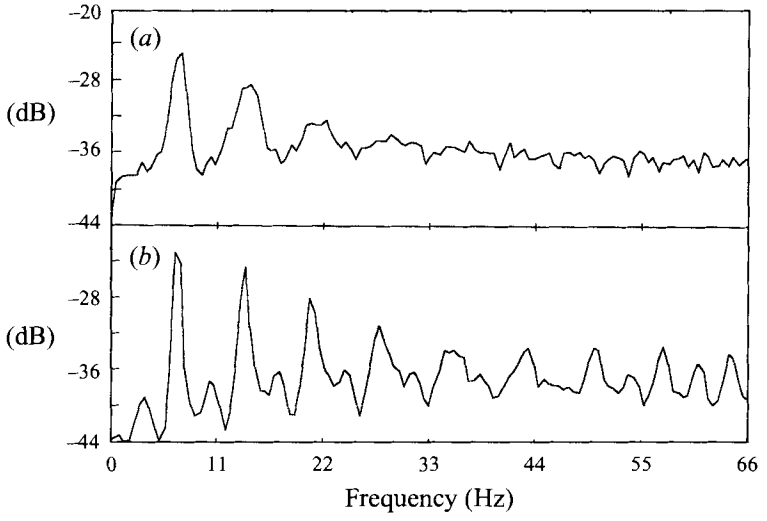

FIGURE 6. Spectra of phase difference ϕ_s from (*a*) experimental data and (*b*) iterates from the averaged return map for nearly periodic modulations of pairing NPMP. Flow parameters the same as for figure 4.

results in a wide spectral bandwidth $b = f_{ex}/2$, which includes all fluctuations between $f_{ex}/4$ and $3f_{ex}/4$ (66–198 Hz) in a_s and between $3f_{ex}/4$ and $5f_{ex}/4$ (198–330 Hz) in a_f. When bandwidth is increased, amplitude estimates include contributions from frequencies other than the fundamental and subharmonic.

In an attempt to find the underlying map function, the data shown in figure 5(*a*) were averaged (as described in Appendix B) and cubic splines were fitted to the averaged points. The results are plotted in figure 5(*b*). Two interesting features are obvious: (i) the function approaches the diagonal very closely (minimum gap is 0.0018π), but does not touch or cross it; and (ii) there is a small region $0.07 \leqslant \phi_n/\pi \leqslant 0.18$ where the function is non-invertible. The first supports the hypothesis that there is no fixed point but instead a small gap through which iterates pass. The second feature meets a necessary condition for chaos: a horizontal dotted line in the inset crosses the function in three places, illustrating the non-invertibility.

Having obtained the map function empirically, this function was iterated numerically to see if there was any correspondence with the experimental data. Time sequences of the phase $\phi_s(t)$ (not shown) from experimental data and iterates of the map function are similar: the number of iterates per modulation cycle is ≈ 20 in both cases. This similarity is further demonstrated by spectral analysis of $\phi_s(t)$, where the modulation frequency seen in the spectrum of experimental phase angles (figure 6*a*) is almost exactly reproduced in the iterates of the map (figure 6*b*): quadratic curve fits locally around the main peak yields $f_{peak} \approx 6.93$ Hz for the experimental data and $f_{peak} \approx 6.95$ Hz for the map iterates. The iterates of the averaged map were analysed using nonlinear dynamics tools, which reveal correlation dimension $\nu \approx 0.96$ and largest Lyapunov exponent $\lambda_1 \approx 0.11$ bits per orbit (b.p.o.). For comparison, calculations using the unaveraged phase data yield $\nu \approx 1.3$ and $\lambda_1 \approx 0.3$ b.p.o. The difference in dimension between the flow and the map should be unity, and this is approximately the case for the unaveraged map; the largest Lyapunov exponents are comparable in the flow ($\lambda_1 \approx 0.25$ b.p.o.) and the map. The difference in dimension is greater than unity between the flow ($\nu > 2$) and the averaged map ($\nu < 1$); this indicates that the dynamics

are not fully captured in the average, which is a type of projection. However, some essential features of the flow are retained: the map dynamics are nearly periodic but actually chaotic (as was the raw data), and the modulation frequency is accurately predicted. Since the averaging process yields a deterministic map, its iterates have no random noise; the good agreement in modulation frequency and chaos characteristics between data and the averaged map indicate that noise plays a minimal role in the dynamics.

Error analysis (presented in Appendix B) shows that the error in ϕ estimates scales on the relative amplitude errors, i.e. the ratios of amplitude errors to amplitudes themselves. The error in the averaged ϕ_s was estimated by evaluating equation (B 4) in bins of width $\phi_s/\pi = 0.01$. This finite bin width introduces an uncertainty (in the error estimate), but this is unavoidable due to the finite amount of data. Taking the amplitude error estimates ϵ_a and ϵ_b to be the standard deviations σ_a and σ_b within each bin, the error limit range is $\epsilon_\phi \approx 0.01\pi$–$0.04\pi$ at various ϕ_s. These limits are larger than the gap, meaning that it is possible that the function does touch or even cross the diagonal. However, small shifts in the curve near the point of tangency would cause large differences in modulation frequency; the exceptional agreement in frequency indicates that the averaged curve (figure 5*b*) must be very close to the true function.

Several features indicate subtle dynamics in this intermittency transition. Specifically, the inset in figure 5(*b*) seems to show a dual near-tangency at phases $\phi_s \approx 0.19$ and 0.22 (with a slightly larger gap in between); dynamically, this would mean that the system would first reach a plateau near one phase for some time, then near the other phase, then jump. This seems to be borne out in figure 3(*b*) for cases (ii) and (iii). Since a_s is closely linked to ϕ_s (because ϕ_s controls the resonant subharmonic growth rate), a similar feature is expected in amplitudes as well. This can be seen to some degree in figure 3(*a*) for cases (ii) and (iii). Even in the a_s return map (figure 4*b*), a second accumulation point can be seen on the diagonal at $a_s \approx 650$, as well as a clearer one at the turning point at $a_s \approx 800$. The accumulation points imply that feedback there is almost phase-locked. We speculate that the initial subharmonic amplitude is higher for one of these two phases than the other but with a lower corresponding growth rate (see §2.3); in both cases the time from initiation to feedback might almost match the subharmonic period (the condition for phase-locking).

The results presented here clearly indicate that the SP–NPMP transition is a tangent bifurcation from a phase-locked periodic state to a phase-varying, nearly quasi-periodic, chaotic state. It further demonstrates the important role of ϕ in the long-time dynamics of vortex pairing. This transition scenario is further supported by a one-dimensional map for ϕ_s dynamics (derived from the concepts of linear instability, subharmonic resonance and feedback; Broze & Hussain 1991) which undergoes tangent bifurcations from a fixed point (e.g. SP) to periodic, quasi-periodic and chaotic (e.g. NPMP) states – all dense in the parameter space.

2.2. *SDP–QCA transition*

The transition from stable double pairing (SDP) to the quarter-harmonic chaotic attractor (QCA) is apparently intermittent, alternating unpredictably between the two states *ad infinitum*. Because of this intermittency, a tangent bifurcation was expected in this transition; therefore, return maps of ϕ_q and a_q were constructed and averaged, similar to the NPMP case. In addition, the scaling exponent of the probability density function of the lengths of periodic segments of the signal was estimated and compared with the scaling of known intermittent models.

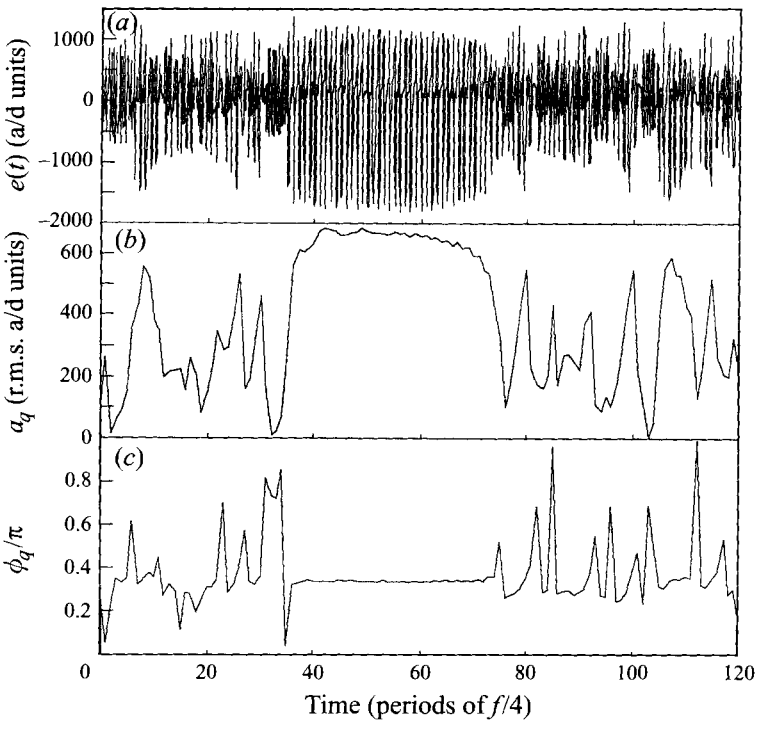

FIGURE 7. (*a*) Time trace; (*b*) quarter-harmonic amplitude a_q; (*c*) subharmonic–quarter-harmonic phase difference ϕ_q for intermittency between stable double pairing SDP and the quarter-harmonic chaotic attractor QCA. $St_D \approx 1.20$, $a_f \approx 1.4\%$, $Re_D \approx 2.3 \times 10^4$, $x/D = 2.0$.

2.2.1. *Phase and amplitude return maps*

In this case where two subharmonic resonances occur (i.e. the pairing of two vortices which themselves result from earlier first pairings), there are four dynamical variables: two amplitudes (a_s and a_q, the subharmonic and quarter-harmonic respectively) and two phase angles (ϕ_s and ϕ_q, the phase differences between fundamental and subharmonic, and between subharmonic and quarter-harmonic respectively). Since both SDP and QCA have high-amplitude quarter-harmonic components, we use a_q and ϕ_q as the variables of interest for analysis. These variables are excellent indicators of periodicity or chaos, as is illustrated below.

A representative hot-wire signal is shown in figure 7(*a*). At each end of the time trace are chaotic oscillations characteristic of the QCA attractor, while the segment in the centre of the trace is nearly periodic with frequency $f_{ex}/4$. (In fact, the slight displacement of adjacent peaks in this segment even indicates a weak $f_{ex}/8$ component.) Phase–amplitude decompositions were performed as described in Appendix B. Figures 7(*b*) and 7(*c*) show a_q and ϕ_q respectively for the time trace displayed in figure 7(*a*). Corresponding to the long periodic segment in the centre of figure 7(*a*), there are segments of high a_q (figure 7*b*) and nearly constant ϕ_q (figure 7*c*), while the chaotic segments have rapidly fluctuating amplitude and phase which are typically not in the range of values seen in the periodic segment. This indicates that these variables are good discriminators of SDP and QCA.

A ϕ_q first-return map was made from these data and is shown in figure 8(*a*). Unlike figure 5(*a*) for NPMP, the broad scatter of experimental data is expected; there seems to be a cross-shape centred on the diagonal at $\phi_q/\pi \approx 0.4$. (Note that figures 8*a* and

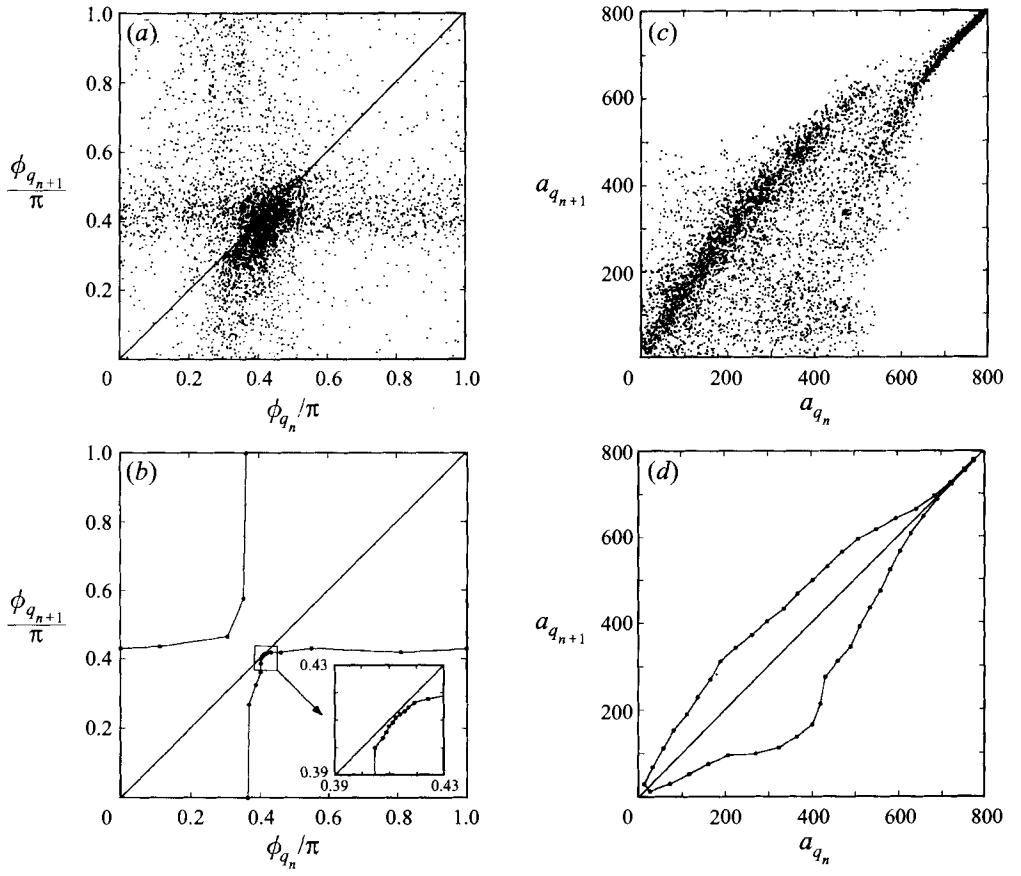

FIGURE 8. (*a*) First-return map of subharmonic–quarter-harmonic phase difference ϕ_q; (*b*) averaged first-return map of ϕ_q; (*c*) first-return map of quarter-harmonic amplitude a_q; (*d*) averaged first-return map of a_q for intermittency between stable double pairing SDP and the quarter-harmonic chaotic attractor QCA. Flow parameters the same as for figure 7.

8*c* show the first 10000 of the 25000 realizations used in the averages.) Although the uncertainty (as seen in the data scatter) is much greater in this case than in the SP–NPMP transition, we constructed an averaged return map assuming that the function enters at the left, moving up and wrapping from π to 0, continuing up toward a near-tangency below the diagonal then moving to the right and wrapping back to the entry point. Since the heaviest concentration of points seems to be associated with the branch below the diagonal but appears to cross over the diagonal due to scatter, all points a distance $\geqslant \epsilon$ above the diagonal were averaged separately from those below (see Appendix B). The result is shown in figure 8(*b*) for $\epsilon = 0.02$. Even with the averaging, the function is not very smooth. The averaged points will shift as ϵ is changed; $\epsilon = 0.02$ was chosen by inspection based on the distance by which the thickest cluster seemed to lie above the diagonal. The figure does show a near-tangency below the diagonal, while the approach above the diagonal is not nearly as close. The position of the function relative to the diagonal, especially in the near-tangent region, is in doubt since ϵ is selected somewhat arbitrarily. However, tests using $\epsilon = 0$, 0.01, 0.02 and 0.05 indeed show that the averaged function never crosses the diagonal; the minimum distances were 0.005, 0.0018, 0.0017 and 0.0015 respectively. These results suggest that a tangent bifurcation has taken place.

A first-return map of a_q (figure 8*c*) was also constructed to see if it provides any insight into this apparent tangent bifurcation. Expecting a loop, points above and below the diagonal were averaged separately to reveal a cycle (figure 8*d*) with a long cusp-like extension along the diagonal at high a_q. Using the Broze-Hussain (1991) model for pairing phase dynamics, amplitude can be extracted as a slaved variable to phase; a return map reveals an amplitude loop (with a similar cusp) near the transition to chaos. The similarities in our data (figures 8*b* and 8*d*) and the model results (as well as other comparisons made in Broze & Hussain 1991) suggest that our model may adequately represent the experimental system in the periodic and transitional regions of the parameter space.

2.2.2. *Type of intermittency*

Although the data are clearly intermittent (based on the observation of time series similar to but much longer than in figure 7), the type of intermittency is unclear. There are several indicators of type, which we describe and compare to our system in the following. First, Pomeau & Manneville (1980) identified three types of intermittency (I–III), defined in terms of map eigenvalues crossing the unit circle: (I) an eigenvalue crosses at $+1$, (II) a complex-conjugate pair crosses, and (III) an eigenvalue crosses at -1. A complex version of the Broze–Hussain (1991) phase map (namely $z = \cos\phi + \mathrm{i}\sin\phi$, where $\phi_{n+1} = \phi_n + 2\pi h/(1+q\cos\phi_n)$) does reveal a pair of complex-conjugate eigenvalues crossing at the point of transition to chaos; hence type-II intermittency is suspected. Second, characteristic frequency changes are associated with each type of intermittency: type I involves a fundamental f_0 which does not change, type II involves f_0 and a new frequency f_1, and type III involves f_0 and $f_0/2$. In our experiments (see BH), SDP has a dominant frequency $f_{ex}/4$ and its harmonics; the transition to QCA leads to sidebands around $f_{ex}/2$ and a broadband around $f_{ex}/4$. The appearance of new frequencies which are not subharmonics seems to rule out types I and III and may indicate type II. Third, associated with each type of intermittency is a universal probability distribution of the lengths τ of periodic segments which has a characteristic scaling exponent; this scaling exponent is investigated in the next subsection.

2.2.3. *Statistics of periodic signal lengths*

It is expected that the lengths τ of periodic segments should follow one of several universal probability distributions, depending on the type of intermittency; the reader is referred to Schuster (1988, p. 98) for details. The distribution should scale as $p(\tau) \sim \tau^{-q}$ for small to moderate $\tau(\tau > 0)$ where q equals $\frac{1}{2}$, 2 or $\frac{3}{2}$ for types I, II or III respectively. As discussed below, the estimated q for our data is close to 2 over a range of excitation amplitudes, indicating a type-II intermittency.

Each realization (i.e. a pair of values a_q and ϕ_q) determined over a period $4/f_{ex}$ is classified as SDP or QCA by using a minimum amplitude threshold and range of acceptable phases. Then the number τ_n of consecutive realizations classified as SDP is counted, a histogram is made of the set of all τ_n, and its scaling exponent q is estimated. An analysis of the effects of phase and amplitude thresholds on scaling exponents is made in the section on intermittency statistics in Appendix B. Data were taken at $St_D \approx 1.20$ for several different a_f, each comprising at least 1.5×10^6 realizations (in blocks of 5×10^4).

The intermittency factor I (fraction of total realizations which do not meet the phase and amplitude criteria for SDP) is shown in figure 9(*a*) as a function of a_f in the transition range. At $a_f \approx 1.26\,\%$, the flow is almost 100 % chaotic and becomes almost

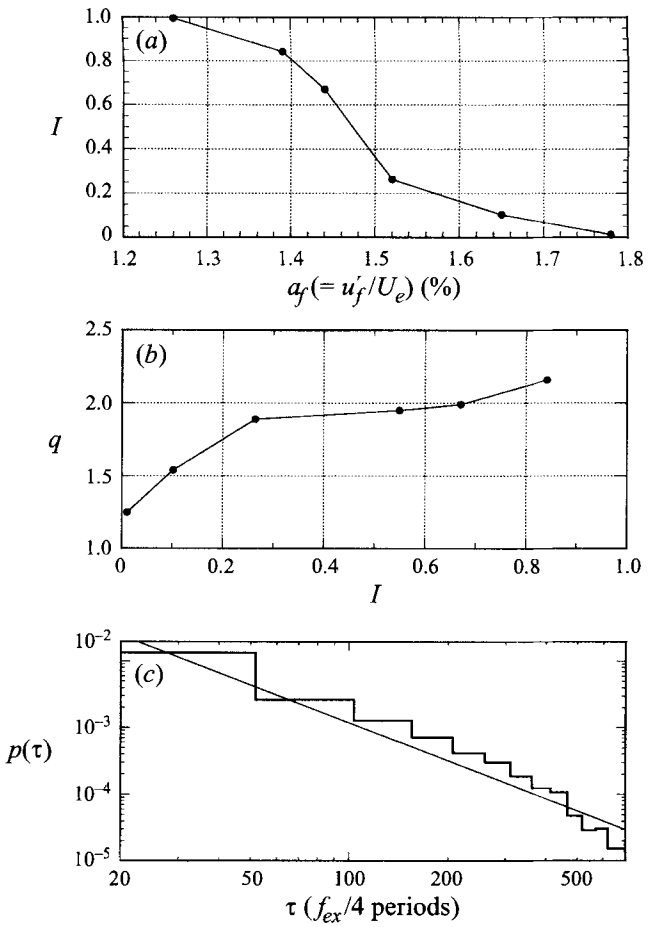

FIGURE 9. (*a*) The intermittency factor I versus forcing amplitude a_f, (*b*) the intermittency exponent q versus I, and (*c*) a representative p.d.f. for the lengths of periodic double pairings at $a_f \approx 1.44\%$ for intermittency between stable double pairing SDP and the quarter-harmonic chaotic attractor QCA. $St_D \approx 1.2$, $Re_D \approx 2.3 \times 10^4$, $x/D = 2.0$.

100% SDP by $a_f \approx 1.78\%$. The intermittency exponent q is shown in figure 9(*b*) as a function of I. For I near zero, q is close to 1.25, but increases with I and levels off near $q \approx 2$ in the range of $0.26 \leqslant I \leqslant 0.84$. For the case $I \approx 1$ ($a_f \approx 1.78\%$), there were insufficient periodic segments to find a valid scaling exponent. Since q represents the power-law decay rate of the p.d.f. of periodic segment lengths, the general trend of q increasing with I is expected: low I means SDP dominates, with more long periodic segments and slower p.d.f. fall-off, while high I means QCA dominates, leaving very few long periodic segments (without a proportional decrease in the number of short periodic segments) and hence faster p.d.f. fall-off. The plateau in q for $0.26 \leqslant I \leqslant 0.84$ indicates that q is independent of I (and hence a_f) over a substantial portion of the intermittency range. And finally, the value of this plateau, $q \approx 2$, coincides with the scaling exponent for a type-II intermittency. A typical p.d.f. (figure 9*c*) for the case $I \approx 0.68$ ($a_f \approx 1.44\%$) shows power-law behaviour (with $q \approx 1.95$) for periodic lengths of up to several hundred quarter-harmonic periods.

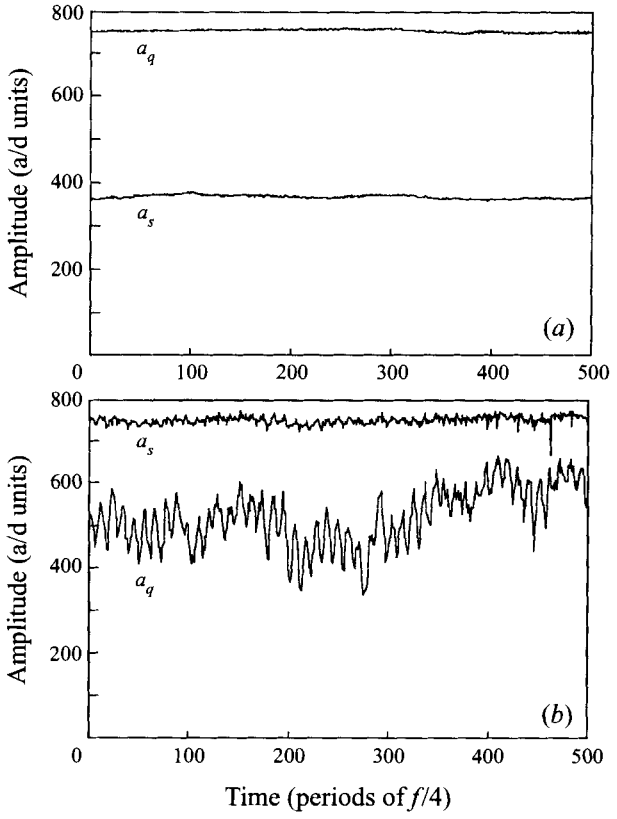

FIGURE 10. Comparison of subharmonic amplitude a_s and quarter-harmonic amplitude a_q as functions of time at $x/D = 2.0$ for (*a*) stable double pairing SDP at $St_D \approx 1.19$, $a_f \approx 2.4\%$, $Re_D \approx 2.3 \times 10^4$ and (*b*) stable pairing with modulated quarterharmonic at $St_D \approx 1.00$, $a_f \approx 0.48\%$, $Re_D \approx 2.7 \times 10^4$.

2.2.4. *Summary*

Based on the intermittency exponent (in addition to the experimental spectra and eigenvalues resulting from our model), the transition appears to be type-II intermittency. Schuster (1988, p. 99) stated that 'Type-II intermittency has (to the best of our knowledge) not yet been found in a real experiment'; subsequently Ringuet, Roźe & Gouesbet (1993) reported type-II intermittency in an experiment involving a heated liquid–gas surface. Hence this is perhaps the first example of type-II intermittency in an open flow and one of the first in experiments.

2.2.5. *SDP–SPMQ transition*

The transition from SP and SDP (see figure 1) goes through the SPMQ state (stable pairing with modulated quarter-harmonic). This is an apparent transition from a periodic state to a periodic state, but in fact it is likely to be two separate transitions: SDP–SPMQ and SPMQ–SP. To illustrate the first transition, figure 10 shows traces of subharmonic and quarter-harmonic amplitudes (a_s and a_q) for SDP and SPMQ. As is apparent, a_q and a_s are both nearly constant for SDP, but a_q becomes (non-periodically) oscillatory for SPMQ. As St_D is decreased, a_s remains stable and a_q continues to fluctuate but with diminishing amplitude until SP is reached. This suggests that the first transition (SDP–SPMQ) may be a tangent bifurcation, while the second

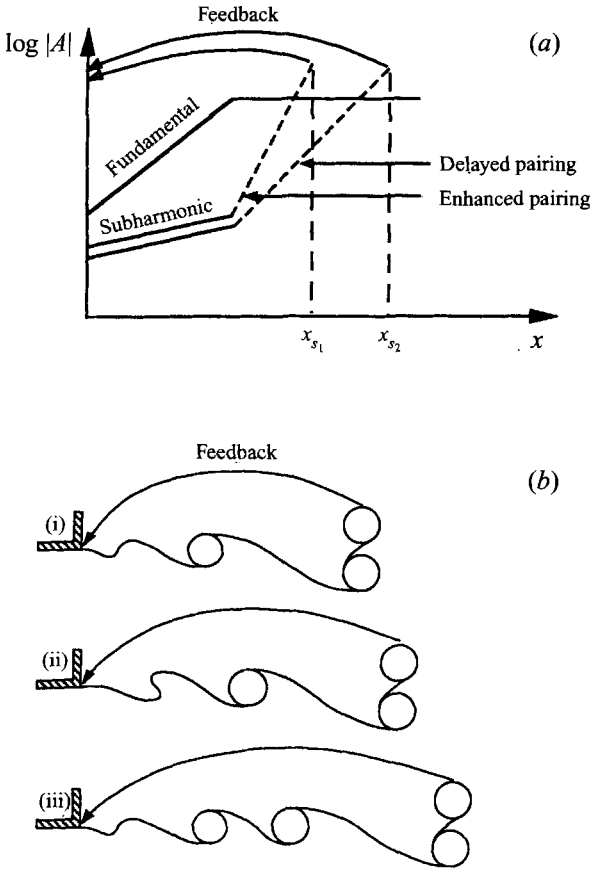

FIGURE 11. (*a*) Conceptual picture of the spatial development of fundamental and subharmonic amplitudes and feedback for two subharmonic phase angles leading to enhanced or delayed vortex pairings. (*b*) Sketches of the vortex configurations for cases when pairing is (i) nearly phase-locked, (ii) somewhat delayed and (iii) delayed such that one vortex escapes pairing.

(SPMQ–SP) may instead be a smooth transition. However, since a_q is not the dominant component and data scatter is significant, this has not been verified by additional analysis.

2.3. *Feedback dynamics and tangent bifurcations*

In order to explain the tangent bifurcations seen, figure 11(*a*) shows a conceptual sketch of the essential system dynamics (namely vortex roll-up, pairing and feedback): *f* and *s* growth, *f* saturation, *f*–*s* resonance, *s* saturation and feedback. The quantities referred to in figure 11(*a*) are the amplitudes of velocity fluctuations at specific frequencies, associated with induced velocity from vorticity fluctuations (e.g. advecting and interacting vortices). A more detailed analysis of the vortex interactions and spatially developing fluctuations connected with subharmonic resonance is given in Husain & Hussain (1995).

As described in BH, the crucial nonlinearity is the ϕ_s-dependent resonant *s* growth rate, which can change the pairing location substantially. The key to periodic pairing is phase-locking; i.e. ϕ_s is the same for each pairing event. This requires that the cycle time (growth–saturation–feedback) τ_{fb} equal the subharmonic period $\tau_s = 2/f_{ex}$. Since feedback itself is almost instantaneous (moving at acoustic speed in a flow with Mach

number $M < 0.10$), τ_{fb} is primarily determined by the evolution from $x = 0$ to the subharmonic saturation location x_s. Assuming (for discussion only) a constant phase speed c, $\tau_{fb} \approx x_s/c$. Since different ϕ_s result in different resonant subharmonic spatial growth rates (Monkewitz 1988), we designate the saturation locations in figure 11(*a*) to be x_{s_1} for the maximum growth rate and x_{s_2} for the minimum growth rate, with corresponding minimum and maximum feedback cycle times τ_{s_1} and τ_{s_2}. (In fact, the minimum growth rate could result in no pairing at all and τ_{s_2} could be indefinitely large, but it is only necessary that $\tau_{s_2} > \tau_{s_1}$.) Thus, it obviously follows that a necessary condition for phase-locking is $\tau_{s_1} \leqslant \tau_s \leqslant \tau_{s_2}$, i.e. the subharmonic period must fall between the maximum and minimum feedback times. It also follows that if $\tau_s < \tau_{s_1}$, phase-locking and periodic dynamics are impossible.

How, then, does the transition from periodic pairing occur? Assume phase-locking for some a_f and St_D. As a_f is decreased, x_s shifts downstream due to the delayed onset of subharmonic resonance (due to delayed f saturation) and a decreased feedback amplitude. If a_f is decreased sufficiently, τ_{s_1} must exceed τ_s and stable (periodic) pairing becomes impossible. This is the case in the SP–NPMP transition. In double pairing, however, there are two subharmonic resonances, and hence there must be two phase-lockings for SDP. Therefore, there can be two transition scenarios: (i) the first resonance remains phase-locked while the phase becomes unlocked in the second resonance or (ii) the first resonance (and, hence, the second) becomes phase-unlocked. The second scenario apparently occurs in the SDP–QCA transition, while the first seems to occur in the SDP–SPMQ transition.

Some essential vortex and feedback dynamics are captured by analysing phase and amplitude maps. Take the case when phase becomes unlocked: successive pairings move further downstream or even do not occur, and thus feedback (i.e. the self-excitation mechanism) should become progressively weaker. The key question is: how then does pairing recur after this? The answer is a jump in phase. In particular, the minimum amplitudes in the NPMP signal (figure 8*a* in BH and case (iii) in figure 2 here) occur when one vortex escapes pairing. Since there are two vortices in each 2π pairing cycle, a skipped vortex should correspond to an overall phase jump of π, as seen in cases (ii) and (iii) of figure 3(*b*) and in the abrupt phase jumps in figure 5. This is shown in figure 11(*b*) (in this schematic, note that roll-up and pairing locations do not match with figure 11*a*): in sketch (i), pairing occurs relatively early in x and the feedback perturbs the second (not yet rolled up) vortex of the two unpaired vortices, leading to their pairing; in sketch (ii), feedback occurs further downstream, perturbing the second vortex again but with some delay which in turn delays their pairing. Finally, pairing occurs so late (sketch iii) that a third vortex is already forming; thus the two vortices nearest the exit will pair, but the one further away has no single vortex to pair with (although it may interact eventually with either the upstream or downstream pair). This skipped vortex is the mechanism by which the system is able to jump from a phase which is unfavourable for pairing to one which is favourable; the upper halves of the loops in the amplitude return maps for NPMP (figure 4*b*) and QCA (figure 8*c*) reflect the reinitiation of pairing and double pairing respectively after having reached very low amplitudes.

Summarizing, the phase-locking/unlocking scenario can qualitatively explain all three observed transitions. Based on data presented in §§2.1 and 2.2, at least two of the three are intermittencies due to tangent bifurcations.

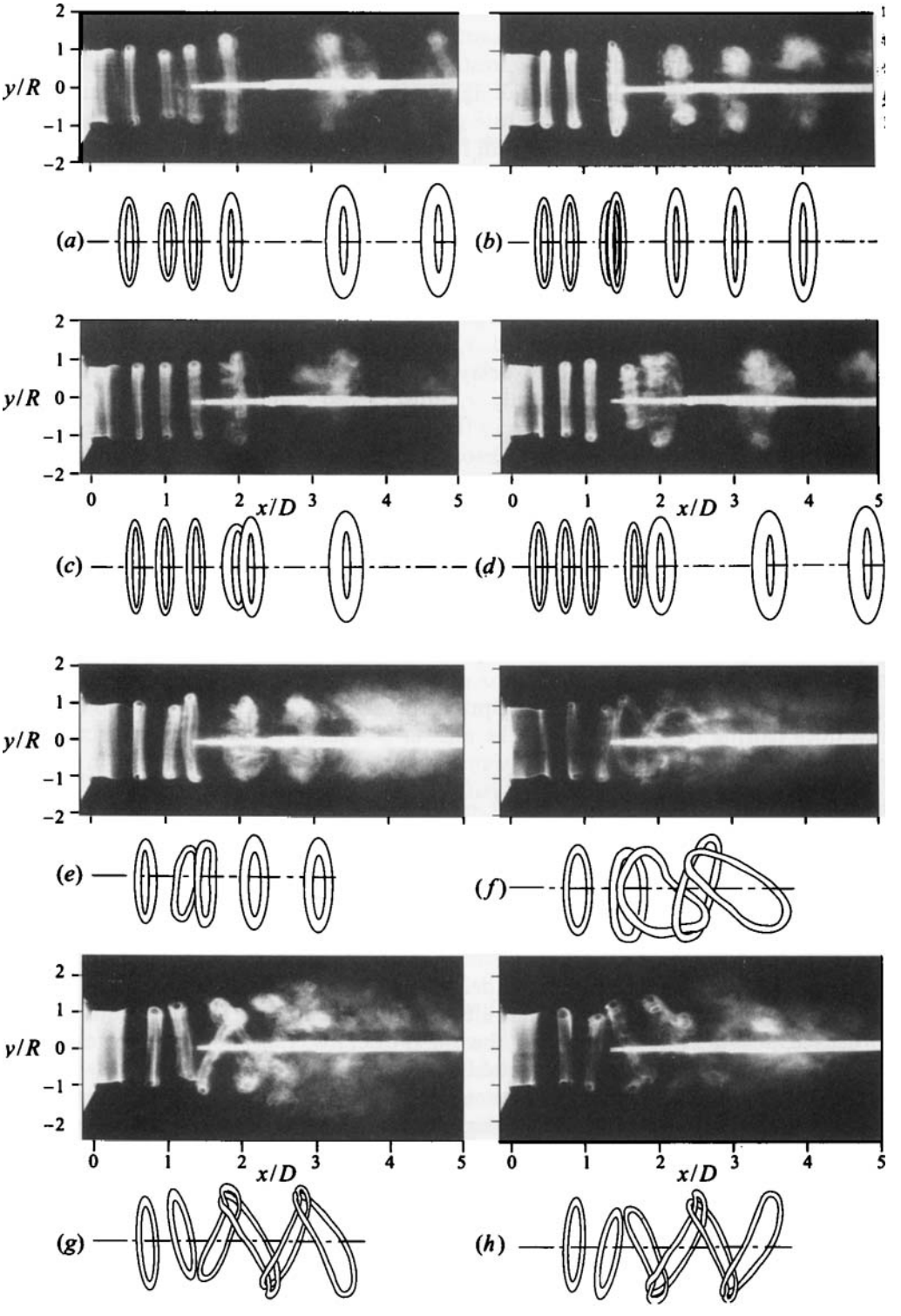

FIGURE 12. Smoke visualization of three flow states at $Re_D \approx 2.3 \times 10^4$ and $St_D \approx 1.20$: SDP at $a_f \approx 2.4\%$, (*a*) Roll-up, pairing and double pairings; QCA at $a_f \approx 1.4\%$; (*b*) roll-up and pairings only; (*c*) roll-up, pairing and delayed double pairing; (*d*) roll-up, pairing and double pairings similar to

2.4. *Visualization of vortex dynamics*

To verify the assumed axisymmetry and phase-locked/unlocked vortex dynamics, three states were visualized at $St_D \approx 1.2$: SDP, QCA and AM (as well as INT). Smoke was introduced through a slit in the nozzle-exit nose cone (shown in the inset of figure 17). Simultaneously, hot-wire anemometry was used to verify the flow state; based on our previous experience, the power spectrum and instantaneous signal were sufficient to identify the state. The flow was illuminated by a floodlight strobed at the quarter-harmonic frequency $f_{ex}/4$ to allow phase-locked observation of double pairings; in addition, we also recorded representative snapshots (not phase-locked) shown in figure 12 along with sketches of the vortex configurations. Figure 12(*a–d*) shows that both SDP and QCA are axisymmetric, while figure 12(*e–h*) shows that AM is intermittently non-axisymmetric. These snapshots (taken at intervals of several seconds or more, much longer than the fundamental period of 4 ms) and our phase-locked visualization are discussed below. The hot-wire probe used to verify the dynamical state can be seen in the figures; we have verified that the presence of the probe does not influence the vortex dynamics. To aid in distinguishing single, paired and doubly paired vortices, note that the normalized wavelength $\lambda/D \approx (2St_D)^{-1}$; hence $\lambda/D \approx (0.4, 0.8, 1.6)$ for $f/f_{ex} \approx (1, 0.5, 0.25)$ at this St_D.

One representative phase of SDP is captured in figure 12(*a*), which is quite similar to the phase-locked coherent structure educed by Bridges & Hussain (1992) in the same facility at a Re_D approximately three times larger (compare with the last panel of their figure 6). Near the exit, the smoke sheet has rolled up into a vortex at $x/D \approx 0.5$. Downstream, a double-pairing interaction is occurring: the vortex at $x/D \approx 1.1$ is shrinking in radius prior to pairing with the vortex at $x/D \approx 1.4$; these will in turn merge with the already-paired vortex seen at $x/D \approx 1.9$. At $x/D \approx 3$–3.8, a doubly paired ring is seen with slight three-dimensionality. Another structure is seen advecting out of the picture at $x/D \approx 4.5$. Tuned, or phase-locked, visualization (strobed exactly at the quarter-harmonic frequency) revealed that the spatial structure is quite repeatable; the vortex positions are seemingly fixed in space by the strobe with only minor small-scale differences between realizations. Slightly detuned strobing revealed successive phases of orderly, periodic single and double pairings.

Three different stages of QCA are shown in figure 12: (*b*) a sequence of pairings without double pairing; (*c*) 3–4 rolled-up vortices without apparent pairing ($x/D \leqslant 1.8$), a paired structure ($x/D \approx 2.1$) and a doubly paired structure ($x/D \approx 3.5$); and (*d*) a double-pairing sequence similar to (*a*): two vortices beginning pairing near $x/D \approx 1$, double pairing underway at $x/D \approx 2$, and a doubly paired structure at $x/D \approx 3.5$. In (*d*), the double pairing at $x/D \approx 2$ shows a lack of axisymmetry (particularly in the trailing structure) and some azimuthal undulations. Unlike SDP, QCA involves non-periodic sequences of vortex interactions in which vortices may or may not pair, and paired vortices may or may not pair a second time. Strobing reveals that vortex interactions are not phase-locked downstream of roll-up; each strobe flash captures a different phase of a chaotic sequence. During SDP–QCA intermittency, strobing showed the vortex positions phase-locking and unlocking as the signal switched from periodic SDP to chaotic QCA.

We had previously speculated (BH) that the AM state involved non-axisymmetric vortex dynamics (perhaps intermittent tilting). This is verified by recent visualization

SDP, AM at $a_f \approx 0.8\%$; (*e*) roll-up and pairings with minimal tilting; (*f*) roll-up and out-of-plane tilting; (*g*) roll-up and in-plane tilting (note enhanced jet spread in this plane); and (*h*) roll-up and in-plane tilting (a virtual mirror image of *g*).

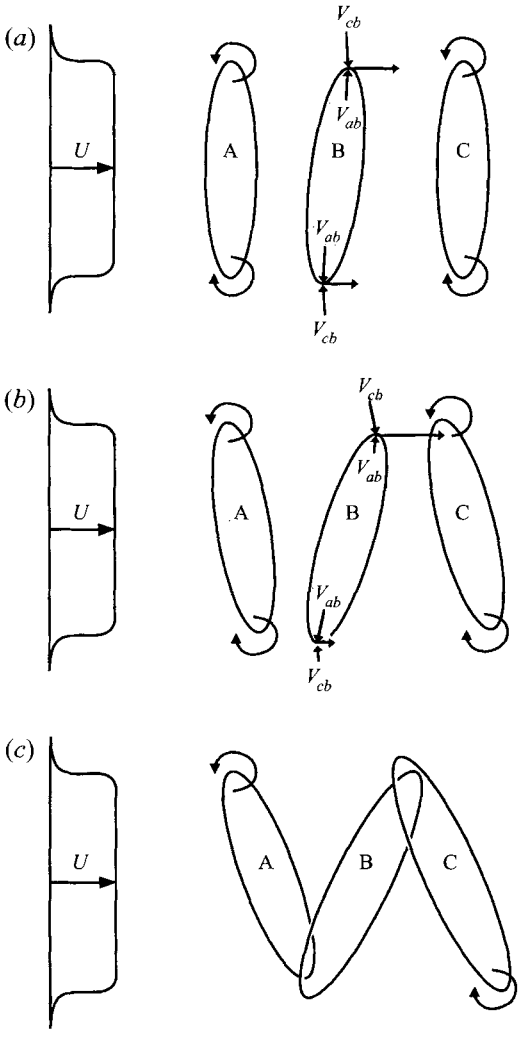

FIGURE 13. The evolution of vortex tilting and entanglement: (*a*) slight tilt of B leads to unequal induced velocities on B, pushing B downward; (*b*) tilt is accentuated since the top of B moves toward the jet centre and hence advects at a higher velocity; the bottom of B decelerates by the opposite effect; and (*c*) B and C meet at the top and A and B meet at the bottom, initiating entanglement.

recorded in figure 12(*e–h*): (*e*) shows slight tilting during pairing, but essentially axisymmetric paired rings downstream; rings are tilted primarily in the plane orthogonal to the picture in (*f*), but are strongly tilted in the photo plane in (*g*) and (*h*). Note the apparent increase in jet spread in the tilting plane (as seen from the spread of smoke in figure 12*g*) due presumably to non-axisymmetric vortex-induced motion. Strobing revealed intermittent tilting and non-tilting, with the tilting plane rotating on a time scale (of the order of a second or longer) much slower than the roll-up time.

These observations raise some questions about the origin and development of tilting modes in jets. The source of the non-axisymmetric disturbances is not clear to us but is presumably low-amplitude transverse modes of the facility settling chamber. However, axisymmetric modes are expected to dominate. Michalke (1971) found for circular jets that the spatial growth rates of the azimuthal modes $m = 0$ and $m = 1$ depend on R/θ, the radius-to-momentum thickness ratio $m = 1$ has a larger growth rate

for small R/θ, but $m = 0$ has a larger growth rate for $R/\theta \gtrsim 6$; note that $R/\theta_e \approx 100$ in our jet, where θ_e is the momentum thickness at the jet exit. Given the larger expected growth rate and initial amplitude (via forcing) of the axisymmetric mode, how can tilting modes be seen so close to the exit? There are two factors which may bear on this question. First, while the amplitude of the fundamental axisymmetric mode is much larger due to forcing, the subharmonic perturbations come only from feedback and are much weaker; hence weak azimuthal instabilities might compete with axisymmetric instabilities more favourably after roll-up. Second, the tilting is apparently an instability of the rings in a jet rather than the jet alone; this can be explained by vortex-induced motion once a tilting perturbation is present. Figure 13 sketches a scenario for the evolution of vortex tilting and entanglement: (*a*) a slight tilt of vortex B leads to unequal velocities induced on B by A (v_{ab}) and by C (v_{cb}), and causes B to move downward; (*b*) tilt is accentuated since the top of B (and bottoms of A and C) moves toward the jet centre and hence has a higher advection velocity (denoted by the horizontal arrows); the bottom of B (and tops of A and C) decelerates by the opposite effect; and (*c*) vortices B and C meet at the top and A and B meet at the bottom, initiating entanglement. Such vertical displacement, tilting and entanglement can clearly be seen in the near field of figure 12(*g–h*).

Thus, the flow visualization has verified several presumed features of the vortex dynamics: (i) (approximate) axisymmetry of SDP and QCA, (ii) phase-locked pairings in SDP and phase-unlocked pairings in QCA, and (iii) intermittent tilting modes in AM.

In the following section, we will present and discuss other interesting transitions, namely hysteresis and the formation of an isolated branch in the experimental bifurcation diagram, where QCA can be reached only by non-smooth parameter changes.

3. Hysteresis

Hysteresis is direct evidence of non-uniqueness of solutions: for the same values of the control parameters, two different stationary states coexist whose manifestation depends on the path in parameter space as well as the initial conditions. We discovered this phenomenon in our flow in the parameter region near the SDP–QCA transition and investigated it in more detail.

3.1. *Hysteresis diagram*

There is hysteresis in the region bounded by $1.1 \leqslant St_D \leqslant 1.4$, $0.007 \leqslant a_f \leqslant 0.07$. Figure 14(*a*) shows the hysteresis region as a_f is increased (lower branch) and decreased (upper branch). The only four states found in this region are stable double pairing SDP, the quarter-harmonic chaotic attractor QCA, aperiodic modulations AM and intermittency INT. The connected lines in the a_f direction indicate that data were taken by varying a_f at fixed St_D; gaps in the lines indicate a change of state. Note that there are two overlapping horizontal lines where hysteresis occurs; the actual (fixed) St_D is midway between these lines. Drawn at two different levels, these indicate various states found when increasing and decreasing a_f; the levels do not indicate different values of a quantified state variable (e.g. dimension or r.m.s. signal component amplitudes). St_D is drawn increasing downward for comparison with the idealized picture given in figure 14(*b*).

At low St_D (1.13 and 1.17), no hysteresis is observed; as a_f is increased, AM undergoes an intermittency transition to QCA, which then becomes SDP via

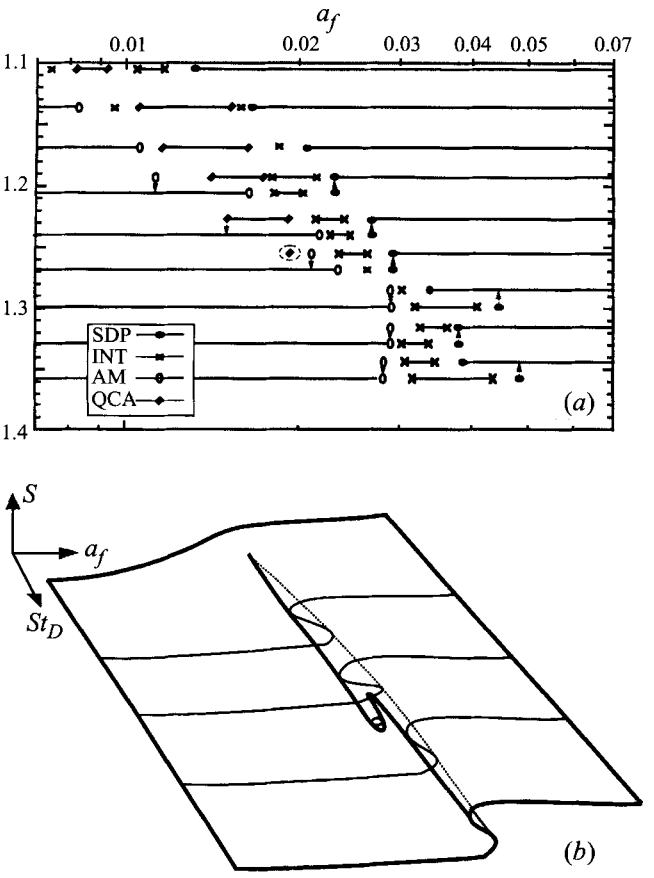

FIGURE 14. (*a*) Flow states in the hysteresis region of a_f, St_D parameter space for $f_{ex} = 264$ Hz showing changes as forcing amplitude a_f is increased (lower branches) and decreased (upper branches). (B) Idealized picture of the local bifurcation surface in this region, where S designates some measure of the system state.

intermittency. For $St_D \geqslant 1.2$, QCA is found only on the descending path. At moderate St_D (1.20 and 1.23) as a_f is increased, AM undergoes a jump to intermittent QCA–SDP, which gives way to SDP, but, as a_f is decreased, SDP changes to QCA via intermittency, followed by a jump to AM. At higher St_D (1.26, 1.29), QCA is not observed as a stationary state when making smooth changes in a_f. AM changes to SDP via intermittency, and there is hysteresis in the values of a_f at which intermittency is seen.

The jump transitions are quite distinct from intermittency. In the observed intermittency, the system switches from one state to the other *ad infinitum* at a fixed value of a_f; when a jump was seen, the system never returned to the pre-jump state. Furthermore, at the jump points, long transients of the (newly) unstable state occurred before the (now) stable state emerged. For example, at the jump at $St_D \approx 1.20$ from AM to QCA–SDP, transient times of the order of 3×10^2 to 6×10^4 periods of $f_{ex}/4$ were observed before the new state emerged. The jump with long transient periods suggests that the transition is a boundary crisis (i.e. the collision in phase space of a chaotic attractor with an unstable periodic orbit, which renders the chaotic state unstable but permits long chaotic transients towards the periodic orbit; see Schuster 1988, p. 182).

At higher St_D (1.26 and 1.29), QCA was observed if changes in a_f were not smooth. By quickly dropping a_f from 0.038 to 0.019 at $St_D \approx 1.26$, stable QCA (marked by a dashed circle on figure 14*a*) was obtained and observed for more than 10^5 periods of $f_{ex}/4$ without transition. This suggests that a stable isolated branch has become separated from the main branch of the bifurcation diagram. At $St_D \approx 1.29$, QCA was obtained by a similar amplitude drop, but it disappeared after a transient time of approximately $10^4 f_{ex}/4$ periods. Since there is no prescribed method to jump into isolated attractors (unlike the quasi-steady parameter changes ordinarily used), it is possible that stable, isolated QCA exists at this St_D but was simply not found in our experiments.

An idealized local bifurcation diagram is shown schematically in figure 14(*b*); S indicates the state of the system. The thick lines represent an outline of the surface, including the cusp, fold and branch. The thin lines denote sections taken by varying a_f at constant St_D, similar to our experiments, while the dotted line shows the fold hidden beneath the upper surface. This sketch is consistent with our data, i.e. with increasing St_D, a cusp is found, followed by a hysteresis fold, an isolated branch and the disappearance of the branch. The shape of this diagram is similar to certain persistent perturbed bifurcation diagrams of the winged cusp (a codimension-3 steady-state singularity in contrast to our unsteady dynamics; Golubitsky & Schaeffer 1985), suggesting that a universal unfolding of low codimension and no more than cubic order might be sufficient to represent these transitions qualitatively.

3.2. *Effect of St_{θ_e} on hysteresis*

The presence of hysteresis suggests the role of additional parameters; one obvious parameter which could effect the dynamics is St_{θ_e} (the Strouhal number based on exit momentum thickness). To investigate the effect of St_{θ_e}, the excitation frequency was changed from $f_{ex} = 264$ Hz to $f_{ex} = 458$ Hz (both being discrete resonance frequencies of the setting chamber). To obtain the same St_D in both cases, U_e and Re_D must be increased by a factor of $458/264 \approx 1.735$. Since $St_{\theta_e} = St_D\, \theta_e/D$, and θ_e/D varies as the inverse square root of Re_D (i.e. $\theta_e/D \approx k/Re_D^{1/2}$, where $k \approx 0.73$ in this facility), then St_{θ_e} in the latter case will be approximately 75% of its value in the base case for an equivalent value of St_D.

Since the hysteresis region is a significant feature of the phase diagram, it was searched for in St_D–a_f space after increasing f_{ex}. Figure 15 shows the results of this experiment in the format of figure 14(*a*), with states for increasing and decreasing a_f shown offset on the same graph. The most striking difference is that the hysteresis region has shifted to higher St_D. For $f_{ex} = 264$ Hz (figure 14*a*), there are QCA hystereses at $St_D \approx 1.20$ and 1.23 and an isolated QCA point at $St_D \approx 1.26$; there is also intermittency hysteresis at higher St_D. For $f_{ex} = 458$ Hz, there is QCA hysteresis at St_D in the range 1.34–1.48 and transient QCA at $St_D \approx 1.54$. No search was made for the isolated branch of QCA.

The values St_D and St_{θ_e} are shown for both cases in table 2. It can be seen that the hysteresis regions fall in the common range $0.005 \leqslant St_{\theta_e} \leqslant 0.006$, but the St_D ranges do not overlap at all; this indicates that the controlling parameter for hysteresis may actually be St_{θ_e}. Further, this would imply that the primary instability in this case is a shear-layer, rather than a jet-column, phenomenon. In this experiment, the shear-layer frequency is closer to its 'natural' frequency than is the jet-column frequency. The St_D of the dominant frequencies in unexcited jets fall in the range 0.3–0.4 (Hussain & Zaman 1981), while this phenomenon has an St_D of three, four or even five times that; in comparison, this range of St_{θ_e} is about half of the commonly observed 'natural'

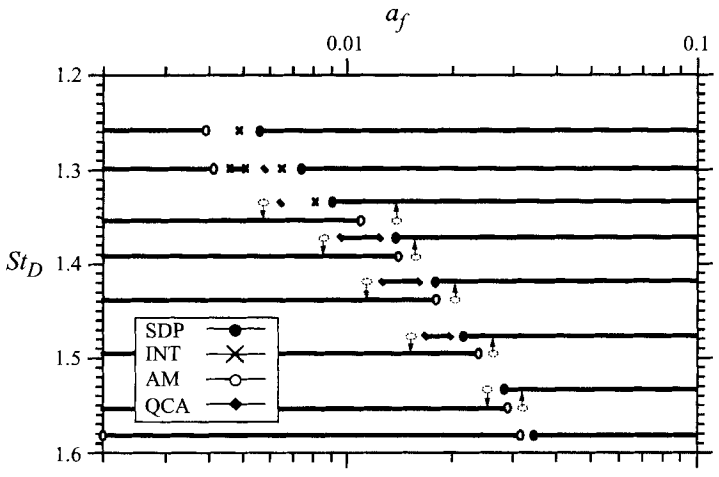

FIGURE 15. Flow states in the hysteresis region of a_f, St_D parameter space for f_{ex} = 458 Hz showing changes as forcing amplitude a_f is increased (lower branches) and decreased (upper branches).

	St_{θ_e}	
St_D	f_{ex} = 264 Hz	f_{ex} = 458 Hz
1.20	**0.0058**	0.0044
1.23	**0.0060**	0.0046
1.26	*0.0062*	0.007
1.30	0.0066	**0.0050**
1.35	0.0069	**0.0052**
1.38	0.0071	**0.0054**
1.43	0.0075	**0.0057**
1.48	0.0079	**0.0060**
1.54	0.0085	*0.0064*

TABLE 2. Relationship between St_D and St_{θ_e} for the hysteresis range; bold indicates in the hysteresis range, italics indicate unstable or isolated QCA.

frequency of shear layers, i.e. $St_{\theta_e} \approx 0.012$. The nature of the primary instability in jets has been debated in the literature for quite some time (Crow & Champagne 1971; Browand & Laufer 1975; Zaman & Hussain 1980; Cohen & Wygnanski 1987). While St_{θ_e} is important in hysteresis, its role in other jet vortex dynamics, e.g. stable double pairing, is not yet established. Studies where a_f, St_D and St_{θ_e} were controlled independently would be of great help in answering this question, but such experiments are difficult in laboratory facilities. Independent control of St_D and St_{θ_e} requires that Re_D and f_{ex} be continuously variable; discrete tunnel resonances make such a frequency variation quite difficult. Furthermore, thorough studies with three parameters instead of two might make experiments prohibitively long.

3.3. *Connections between hysteresis and vortex dynamics*

It appears that the different hysteresis branches (figure 14) may define regions where (i) mixed axisymmetric and tilted vortex dynamics occur (lower branch) and (ii) only axisymmetric dynamics occur (upper branch). Simultaneous visualization and velocimetry by Berger (1993) in another UH facility reveal that aperiodically

modulated states (called 'AM' in BH), found for $St_D > 1$ at a_f less than that for SDP, have intermittent tilted and untilted vortex rings. This was later confirmed in our facility. As discussed in §2.4, it is clear that vortex rings in jet flow can be susceptible to a tilting perturbation. Given this susceptibility, the evolution of the vortex configuration after roll-up depends on whether axisymmetric or non-axisymmetric perturbations dominate.

This competition (between types of perturbations) can be used to explain the hysteresis. A certain level of axisymmetric perturbations (i.e. a_f) is required to establish SDP. However, once established, SDP augments the axisymmetric forcing with axisymmetric feedback from the first and second pairings, thus increasing the level of axisymmetric perturbations above that required for axisymmetric dominance without an increase of a_f. Therefore, it would be possible to decrease a_f (by some amount) without losing axisymmetry. Hence, the hysteresis would be due to the difference in the higher a_f required to *establish* axisymmetric vortex dynamics and the lower a_f required to *maintain* them once they were established.

To summarize, we have found hysteresis and investigated its dependence on flow parameters, including the auxiliary parameter St_{θ_e}. In addition, we have provided a tentative explanation for hysteresis in terms of vortex dynamics. Next, we present measurements to verify that our dynamical system is indeed temporal in the transition region of the jet.

4. The spatial extent of the dynamical system

The results presented in BH and in this paper are based on the assumption that the dynamical system is temporal rather than spatio-temporal, enabling an understanding of the dynamics from single-point measurements alone. This temporal assumption implies that the dynamics must necessarily be coupled over an extended region. The ideas of 'temporal' and 'separable' dynamics are related; both imply that the dynamics can be represented by a countable (preferably finite) number of ordinary differential equations (ODEs) associated with spatial basis functions. This concept is implicit in dynamical modelling approaches using single-point data (e.g. Noack, Ohle & Eckelmann 1992). On the other hand, 'spatio-temporal' and 'non-separable' are not synonymous: spatio-temporal indicates that the applicability of the basis functions is spatially limited because the dynamics in different regions are not well coupled. This does not necessarily imply non-separability; local spatial bases might possibly permit description using temporal ODEs.

Since the predominant dynamics are vortex roll-up and the first and second pairings, for temporal dynamics this coupling must extend at least as far as the completion of pairings. In BH, it was shown that the subharmonic saturates for SP by $x/D \approx 2$, and the quarter-harmonic saturates by $x/D \approx 3$ for SDP and $x/D \approx 4$ for QCA; these data conform well to the coherent structures educed in Bridges & Hussain (1992) for SP and SDP.

Spatial correlation is typically used to measure spatial coupling (Hohenberg & Shraiman 1989; Cross & Hohenberg 1993). However, in spatially developing flows, the relative amplitudes of dominant frequency modes change with axial position, causing correlation to decay with x/D even though the development of these spectral components individually may be perfectly spatially coupled. In these cases, a more meaningful measure of spatial coupling is linear coherence $\gamma^2_{x_1x_2}(f)\,(\equiv |G_{x_1x_2}(f)|^2/(G_{x_1x_1}(f)\ G_{x_2x_2}(f))$, where G is the auto- or cross-spectrum and x_1 and x_2 are measurement locations), which can be thought of intuitively as a spectrum of

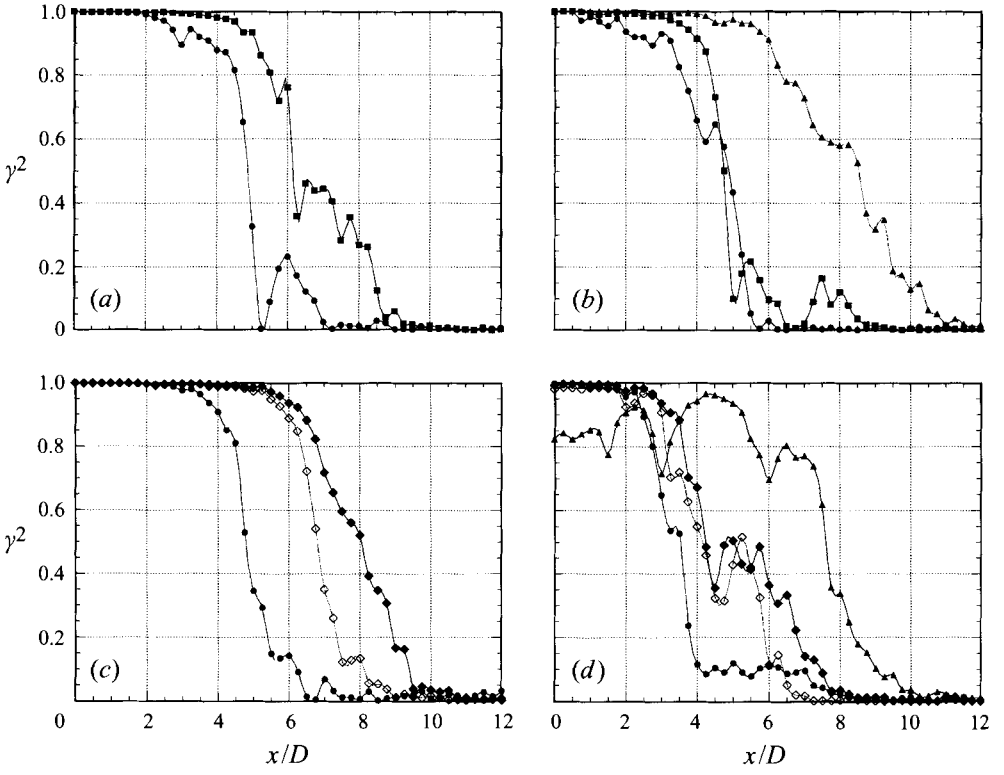

FIGURE 16. Coherence measurements as a function of downstream distance for dominant frequencies (●, fundamental; ■, subharmonic; ◇, lower subharmonic sideband; ◆, higher subharmonic sideband; ▲, quarter-harmonic) for (*a*) SP at $St_D \approx 0.85$, $a_f \approx 2.9\%$, $Re_D \approx 3.3 \times 10^4$; (*b*) SDP at $St_D \approx 1.20$, $a_f \approx 2.4\%$, $Re_D \approx 2.3 \times 10^4$; (*c*) NPMP at $St_D \approx 0.68$, $a_f \approx 3.4\%$, $Re_D \approx 4.0 \times 10^4$; and (*d*) QCA at $St_D \approx 1.20$, $a_f \approx 1.4\%$, $Re_D \approx 2.3 \times 10^4$.

correlations at each frequency. If the dominant frequencies remain coherent over an extended distance, one can consider the dynamics to be spatially coupled and hence temporal. Linear coherence can decay when the flow has nonlinear interactions (Miksad, Jones & Powers 1983; Ritz & Powers 1986); in this case, bicoherence (or even higher order) can be estimated also to show nonlinear coupling. However, to demonstrate coupling it is sufficient to estimate linear coherence. A detailed investigation of the use of linear and nonlinear coherences to distinguish temporal and spatio-temporal domains in spatially developing flows is the subject of a current investigation.

Coherence was measured for four cases: SP, SDP, NPMP and QCA. A fixed probe was placed in the potential core at $x/D \approx y/D \approx 0.2$, upstream of vortex roll-up in all cases and slightly off centreline to avoid interference with the traversing probe. To minimize downstream disturbances (e.g. a shear-layer tone originating from the fixed probe), a special long-prong probe was used and placed such that only the prongs, and not the probe body, was in the flow. A second probe aligned with the axis was traversed down the jet centreline out to $x/D = 12$. These probes were simultaneously sampled and coherence was calculated; these results are shown in figure 16 and are discussed below. The coherence threshold between 'coupled' and 'uncoupled' is somewhat arbitrary; for purposes of discussion, we use a coupling threshold of $\gamma^2_{x_1x_2}(f) = 0.5$.

For SP, only one pairing typically occurs; thus only coherences at the fundamental

(f) and subharmonic (s) frequencies are shown (figure 16a). Coupling extends to $x/D \approx 5$ for f and $x/D \approx 6$ for s; both of these are well beyond the s saturation location of $x/D \approx 2$. Coupling of the quarter-harmonic (q) for SDP (figure 16b) extends even further, beyond $x/D = 8$. For the chaotic cases, one might expect that coupling would decay earlier in x, but this does not seem to be the case. Figure 16(c) for NPMP shows that the subharmonic modulation sidebands actually remain coherent further downstream (out to $x/D \approx 7$–8) than s does for SP. In NPMP, the modulations set in due to a loss of phase-locking in the feedback; this in turn causes a delay in the completion of pairing and, hence, extends the coherent region. Even in the chaotic double-pairing QCA, coherence in the quarter-harmonic band (γ_q) remains above the threshold beyond $x/D = 7$ (figure 16d), showing only a small decrease in the size of the coupled domain. Notably, γ_q oscillates in space and is actually lower at the origin than it is downstream (e.g. $x/D \approx 4$). This indicates that the second pairing is becoming phase incoherent, possibly due to the onset of intermittent vortex tilting (discussed in §3.3) or azimuthally distorted rings. The reference probe, placed off-axis at $y/D \approx 0.2$, will sense variations in induced velocities due to non-axisymmetries that the centreline probe cannot detect.

In all four cases, the results show that couplings at the dominant frequencies extend well beyond their respective saturation locations (roughly twice as far from the exit, or more). This confirms our assumption that the dynamical system is temporal in the region under consideration.

5. Concluding remarks

The relatively simple transitions observed in this flow system, and the periodic and chaotic attractors discussed in BH, combine to confirm the existence of a temporal dynamical system in the transition region of forced jets and indicate that it may be possible to construct low-dimensional models for this system. It is remarkable that this occurs in a convectively unstable, physically open flow, where sensitivity to noise and the absence of physically imposed global length and time scales could increase disorder drastically. These experimental results clearly demonstrate that dynamical systems exist in open flows and that dynamical systems theory is relevant to open flows.

One important question is how these measurements can give insight into the coherent structure dynamics in jet transition. Details of individual vortex formation and pairing have been studied in both numerical simulations and phase-locked experimental measurements; these are not the current objectives. The objective here has been to study the long-time behaviour of sequences of vortex formations and interactions: what dynamical states occur, where do they occur in parameter space, are they low-dimensional and deterministic, how do transitions occur between states, and might it be possible to describe these via a dynamical system, hence permitting models for flow prediction and control? Prediction and control of turbulence phenomena such as entrainment, mixing, combustion, drag and noise is a primary motivation for our interest in dynamical systems. In what follows, we review our conceptual dynamical system and relate it to vortex dynamics.

The conceptual dynamical system (described in BH) involves the initially independent exponential growth of two or more harmonically related instability waves followed by one or more subharmonic resonances and feedback. The initial perturbation at the fundamental frequency comes from forcing; the subharmonic/quarter-harmonic perturbations are initiated by feedback from vortex pairings downstream. As the fundamental wave reaches the nonlinear stage and saturates, a

vortex forms. Subharmonic resonance begins when the fundamental reaches a critical amplitude, and the resonant growth rate depends on the phase angle between the fundamental and the subharmonic. The subharmonic wave is associated with the interaction (i.e. mutually induced motions and eventual merger) of vortex pairs. The acceleration of vorticity during pairing causes feedback, i.e. pressure fluctuations transmitted to the jet exit. At some stage of vortex pairing, feedback reaches its maximum amplitude. This comprises one cycle of the long sequence mentioned above.

Why is vortex pairing periodic or chaotic? Since forcing controls the evolution of the fundamental (i.e. vortex roll-up), the flow controls the subharmonic evolution through feedback. As described in §2.3, there are only two possibilities in the initiation–growth–saturation–resonance–feed-back scenario: phase-locking or phase fluctuation. Phase-locking makes the pairings periodic, guaranteeing the same resonant growth rate, subharmonic saturation location and feedback amplitude in each cycle. When phase becomes unlocked, the frequency and amplitude of the signal modulates when measured at a point as done in our experiments. Phase fluctuation implies that the pairing location moves upstream or downstream from one cycle to the next. These fluctuations can be periodic or chaotic; our results here indicate that phase fluctuation (and, hence, the associated spatio-temporal evolution of vortex pairing) is both deterministic and low-dimensional.

The results presented here and in BH clearly demonstrate the existence of a low-dimensional dynamical system in the transition region of an axisymmetric jet. It seems clear that the system depends crucially on the vortex interactions in this region, particularly vortex pairings due to subharmonic resonance. Further studies, employing perhaps phase-locked measurements and/or simultaneous visualization and velocity/vorticity data acquisition, will be necessary to connect more conclusively the vortex dynamics and the nonlinear dynamical system. Moreover, this discovery of temporal chaos in a convectively unstable, physically open flow makes it possible to explore the transition from temporal to convective or spatio-temporal chaos by using noise to break the feedback loop which closes the dynamics. Thus, we may be able to move closer to the goal of describing and controlling spatio-temporal chaos in open flows.

The authors are grateful to Professor Vladimir Shtern for fruitful discussions, Satish Narayanan for a careful review of the manuscript, Professor Hyder Husain for help in flow visualization and Bill Berger for figure preparation. This work was supported by the Office of Naval Research grant N00014-89-J-1361.

Appendix A. Facilities, equipment and procedures

A.1. *Facilities*

The experiments were performed in a jet facility within a large anechoic chamber, which is extensively documented in Bridges & Hussain (1992). The overall layout is shown in figure 17 and is described below; letters in parentheses refer to those in the figure. The chamber (K) is a ventilated and air-conditioned concrete box set on 44 air bearings, with its 0.3 m thick walls (R) lined with a copper plate (S) to shield from electromagnetic interference and covered by fibreglass wedges (T). The wedges are 1 m long, giving the chamber an ambient sound level of 35 dB above 100 Hz; most of the sound is transmitted through the jet pipe from the laboratory outside the chamber. The inside dimensions of the chamber from wedge tip to wedge tip are 7.6 m × 5 m × 5 m. Air feeding the jet originates at an inlet (A) in the air-conditioned room which contains

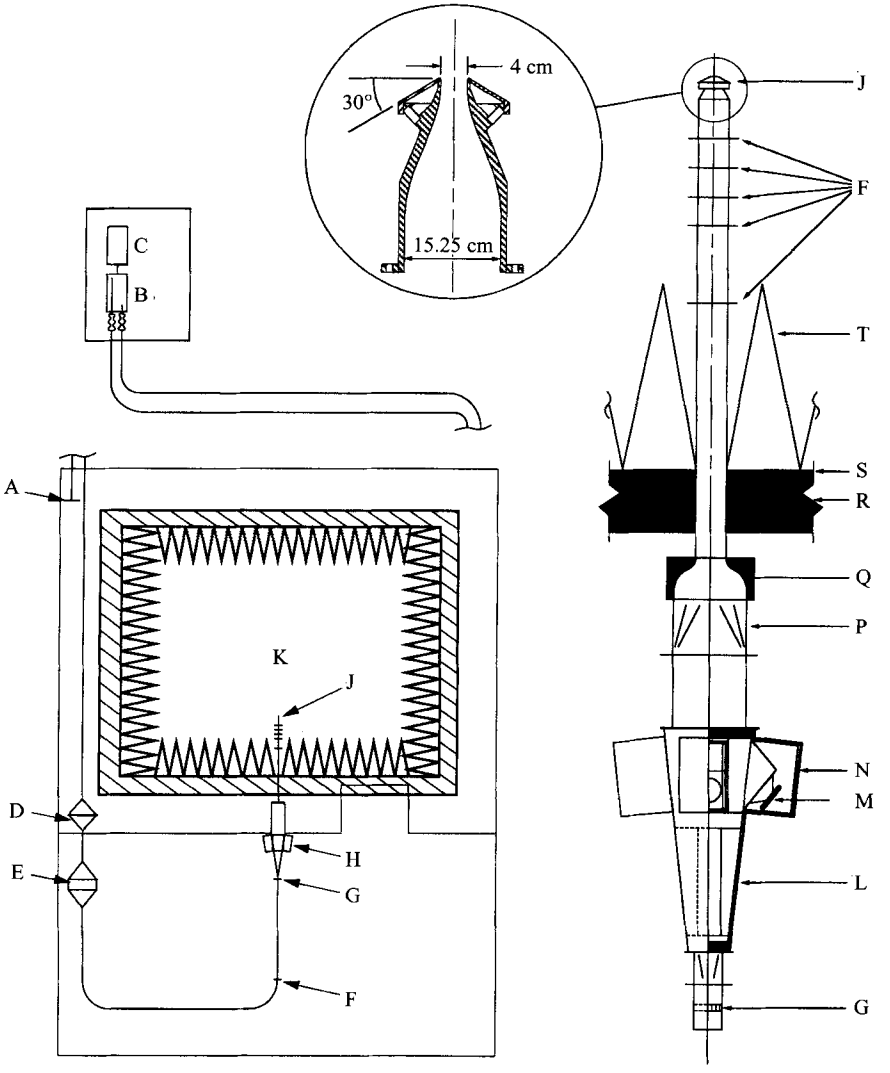

FIGURE 17. Anechoic chamber and jet facility, including: A, air intake; B, compressor with mufflers and vibration isolating couplings; C, DC, motor; D electrostatic filter; E, heat exchanger; F, screens; G, honeycomb; H, bulk excitation device; J, nozzle; K, anechoic chamber; L, diffuser; M, speaker; N, speaker housing; P, square-to-round section; Q, contraction; R, chamber wall; S, copper plate for electrical shielding; T, fibreglass wedges.

the anechoic chamber; it is piped to a 7-stage blower (B) driven by a 40 h.p. DC motor (C) and located outside the building, its outlet being connected to the nozzle in the anechoic chamber via a 77 m long iron pipe of 15.25 cm diameter. Mufflers and vibration isolation couplings located on each side of the blower minimize the transmitted sound and vibration. Between the blower and nozzle are several flow conditioning devices. An electrostatic filter (D) removes any dust or dirt (95% of 2 μm particles) which might damage hot-wire probes. A cooling coil (E) allows the air to be brought back to room conditions for accurate hot-wire measurements. Large-radius elbows (1 m radius) are used at all bends to minimize secondary flow. Seven screens (F) (24 and 40 mesh) and one honeybomb section (G) (0.48 cm cell, 5.08 cm thick) remove

any asymmetry and swirl of the flow and are shown by short line segments between the last bend and the nozzle (J). Machined from solid aluminium stock, the nozzle has a 15.25 cm inlet diameter and a 4 cm exit diameter; the contraction profile is a third-order polynomial with one-half-radius straight sections at both ends.

The DC blower motor is controlled by a Polyspede HP-3 Adjustable Speed Drive System, with adjustments for speed regulation, torque limits and acceleration. At low speeds, the controller 'hunts' for the set point and introduces some low frequency oscillations of the blower (≈ 0.3 Hz), but this is not significant at jet speeds $U_e \geqslant 5$ m s^{-1} ($St_D < 2$); in this study, the speed range used was $7 < U_e < 21$ m s^{-1}. This frequency is three decades lower than the excitation frequency and at least one decade below the lowest observed modulation frequencies.

Bulk excitation (i.e. a longitudinal perturbation added to the mean flow) was provided through the walls of the diffuser (L) by four speakers (M) angled downstream. Perturbations from the speakers pass through a wire mesh and cloth screen which are flush with the walls of the diffuser and provided to prevent disturbance of the flow by the openings of speaker housings (N) into the diffuser. The transfer function of this facility between the speakers and the jet nozzle was reported by Bridges (1990).

A.2. *Parameters*

Because of discrete-frequency tunnel resonances, it is not possible to vary St_D smoothly by changing frequency without simultaneously changing a_f substantially; hence f_{ex} was fixed and St_D was varied by changing U_e. The excitation frequency used in all cases was 264 Hz (with the exception of data presented in figure 15, where $f_{ex} = 458$ Hz); this is a resonance frequency of the jet settling chamber, permitting higher excitation amplitudes.

Note that varying St_D (by changing U_e) also varies Re_D ($\equiv 2.74 \times 10^3/St_D$ for $f_{ex} =$ 264 Hz and $D = 4$ cm). However, these experiments are conducted in the transition region of a laminar-exit, top-hat-profile jet, where Re_D has little effect on the dynamics (e.g. the preferred mode or stable pairing frequencies). Stability theory suggests that viscous jets become unstable at very low Re (e.g. $Re_{cr} \approx 4$ in Bickley's jet, cf. Drazin & Reid 1985, §31.9, $21.8 < Re_{cr} < 55.3$ for viscous round jets with various initial profiles and azimuthal wavenumbers; Kambe 1969; Mollendorf & Gebhardt 1973; Lessen & Singh 1973; Morris 1976). The Re_D range ($1.8 \times 10^3 < Re_D < 5.5 \times 10^3$) in our experiments is well above the theoretical stability limit for jets. Hence Re_D is not used as a primary control parameter. The most notable effect of Re_D is on θ_e and hence on St_{θ_e} (an auxiliary control parameter discussed in §3.2).

A.3. *Data acquisition*

Data for analysis were obtained using hot wires. A long-prong probe was placed in the nozzle exit plane at approximately a 30° angle to the jet axis at $y/R \approx 0.4$ such that the probe body was out of the flow to avoid shear-layer tones (Hussain & Zaman 1978). This reference probe was used to measure u_f' and U_e. A measurement probe (seen in figure 12) aligned with the jet axis was placed on the centreline in the jet potential core at axial locations in the range $1.5 \leqslant x/D \leqslant 3.0$; all data presented were taken at $r/D = 0$. As discussed in §4, any measurement location is adequate so long as it is sufficiently far downstream to register fluctuations due to pairings but within the potential core so that the probe captures the footprints of large-scale structures without the effects of high shear-layer turbulence. Velocity was measured using AA Lab hot-wire anemometers sampled using a 12-bit analog-to-digital converter controlled by a MassComp 500 lab computer. Spectra were computed using an Ono-Sokki CF920

two-channel, 16-bit digital spectrum analyser. For more details of experimental facilities, laboratory equipment and computers, see BH and Bridges & Hussain (1992).

A.4. *Flow properties*

The exit velocity profile is top-hat, with D/θ_e in the approximate range 186–323. At all velocities used, the exit-centreline total r.m.s. velocity fluctuations (excluding excitation) are $u'/U_e < 0.1\,\%$, boundary layer profiles correspond well to the Blasius profile, and boundary layer peak total r.m.s. velocity fluctuations are $u'_p/U_e < 0.5\,\%$. Thus the nozzle exit boundary layer remained laminar at all velocities. Based on hot-wire velocimetry and flow visualization, the length of the laminar core is 5–8 diameters.

Appendix B. Decompositions, averaged maps and intermittency statistics

B.1. *Phase–amplitude decompositions*

From subharmonic resonance theory and experimental observation, it is obvious that the key dynamical variables are the component amplitudes a_s and a_q and phase differences ϕ_s and ϕ_q. Decomposition of the signal into these variables is useful for two reasons: (i) the key variables (perhaps a subset of these four) may be identifiable when they are viewed separately rather than in combination and (ii) discrete variables makes visualizing attractors more comprehensible by reconstructing them in a lower dimension. The signal is assumed to have the following form:

$$f(t) = a_f \cos(2\pi f_{ex}\, t + \phi_1) + a_s \cos(\pi f_{ex}\, t + \phi_2) + a_q \cos(\pi f_{ex}\, t/2 + \phi_3), \tag{B 1}$$

where ϕ_1, ϕ_2 and ϕ_3 are the phases of the fundamental, subharmonic and quarter-harmonic waves with respect to an arbitrary phase reference. This is arbitrary because the signal is divided into segments $\tau = 2/f_{ex}$ (if the quarter-harmonic can be neglected, i.e. for $St_D \leqslant 0.95$ approximately) or $\tau = 4/f_{ex}$ (for $St_D > 0.95$ approximately), and the instant that sampling began was not triggered on any particular phase of any signal component. This arbitrariness is removed, however, by taking differences between phases. For two frequencies f_m and f_n with phases ϕ_m and ϕ_n, phase difference can be defined in a number of ways. For this work, we define

$$\phi_{mn} = \phi_n - (f_n/f_m)\,\phi_m. \tag{B 2}$$

For example, $\phi_s = \phi_2 - \frac{1}{2}\phi_1$. Alternative definitions include multiplying the right-hand side of (B 2) by $-1, f_m/f_n$, or both. Any of these definitions is correct; only consistency is necessary.

Operationally, amplitudes and phases are determined in the following way: (i) the signal is subdivided into segments of length τ; (ii) in each segment, the real and imaginary components of all desired frequencies are computed using discrete Fourier transforms; and (iii) amplitudes and phase differences are computed using $a = (a_r^2 + a_i^2)^{1/2}$ and $\phi = \arctan(a_i/a_r)$. Using these data, various return maps can be made to reconstruct attractors.

Errors can enter into the real and imaginary components either (i) through bandwidth or (ii) if the segment length is not an integer multiple of the period of the dominant frequency. In case (i), for example, if $\tau = 2/f_{ex}$, the bandwidth $b = f_{ex}/2$. This means that the Fourier sums will include all fluctuations from $f - f_{ex}/2$ to $f + f_{ex}/2$, introducing an error. To decrease bandwidth requires increasing τ, thus making the measurements an average rather than a near-instantaneous value. For case (ii), care was taken to ensure that the segments were exactly one subharmonic or quarter-harmonic period, eliminating such an error.

In order to estimate phase error, one must analyse the defining equation. Phase was computed from the following formula (substituting the phase definition into equation (B2)):

$$\phi = \arctan\frac{b_i}{b_r} - \tfrac{1}{2}\arctan\frac{a_i}{a_r}, \tag{B 3}$$

where a and b are fundamental and subharmonic amplitudes respectively, and subscripts i and r refer to imaginary and real. The error ϵ_ϕ in ϕ, assuming equal errors in real and imaginary components, is given by

$$\epsilon_\phi = \left(\frac{\epsilon_b^2}{(b_r^2(1+u^2))} + \frac{\epsilon_a^2}{(4a_r^2(1+v^2))}\right)^{1/2}, \tag{B 4}$$

where u and v are ratios of the imaginary and real components of b and a respectively. Thus, if one can estimate the errors in amplitude components, one can estimate the phase error. For our averages, we assumed that the standard deviation of the amplitudes within each bin was an indicator of the error. This is certainly an upper bound, since the averaging bins are of finite width and there will be a variation of the true amplitudes within the bins themselves.

B.2. *Averages of first-return maps*

The first-return maps of the phase difference ϕ were averaged to try to find underlying map functions. The averages are described below for two cases.

For NPMP, the data in figure 5(*a*) were averaged as follows: (i) ϕ was unwrapped so that points in the ranges $0.35 \leqslant \phi_n/\pi \leqslant 1.0$, $0 \leqslant \phi_{n+1}/\pi \leqslant 0.25$ were shifted up by 1; (ii) the coordinates were rotated by $-\pi/4$; (iii) averages of abscissa and ordinate were carried out for points falling in small bins of the rotated abscissa; (iv) the averaged points were rotated back to the original coordinates; and (v) ϕ was wrapped again and plotted in figure 5(*b*). By rotating the coordinates by $-\pi/4$, the crucial near-tangent region becomes horizontal, and errors in the ordinate introduced by averaging over finite bins are minimized. Care was taken to size the bins so that each average was carried out over at least 100 points; the minimum and maximum number of points per bin were 104 and 590 respectively. Each bin in the region near the diagonal had at least 397 points ($\geqslant 5\%$ of 7893, the total number of points).

For SDP–QCA intermittency, all points at a distance $\geqslant \epsilon$ above the diagonal were averaged separately from those below, and averages were obtained for different values of ϵ. This was done since it was not clear *a priori* where to separate the upper and lower branches of the return map. The data in figure 8(*a*) were averaged in the following way: (i) all points more than ϵ above the diagonal are unwrapped to the right by adding 1 to the abscissa (i.e. $\phi \rightarrow \phi + \pi$); (ii) the data are rotated by $-\pi/4$; (iii) the data are averaged in bins of about 1000 points; (iv) the data are rotated by $+\pi/4$; and (v) the data are wrapped again before plotting in figure 8(*b*). A similar rotation–averaging–derotation was done (for data above and below the diagonal separately) to obtain the averaged a_q return map (figure 8*d*); equisized bins were used to ensure uniform coverage of the loop, with at least 75 points in each bin.

B.3. *Intermittency statistics*

Since the results may be sensitive to the choices of amplitude and phase thresholds, some studies of these thresholds were made. Figure 18(*a*) shows the estimated probability density function (p.d.f.) of a_q for three different forcing amplitudes: (i) $a_f \approx 1.26\%$ (almost all QCA), (ii) $a_f \approx 1.44\%$ (mixed QCA and SDP), and (iii)

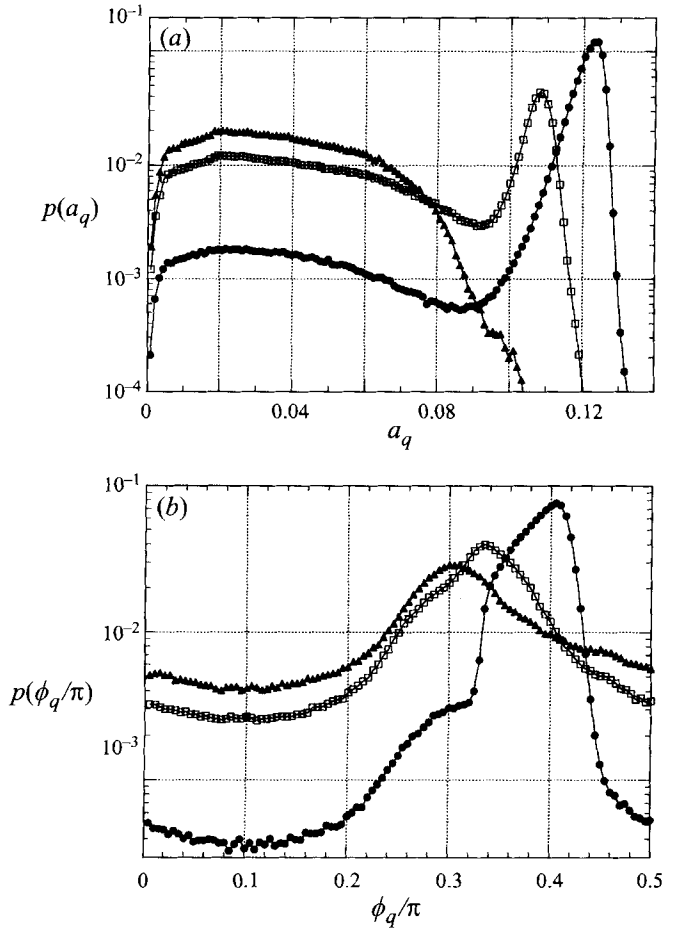

FIGURE 18. Estimates of the probability density functions for (*a*) quarter-harmonic amplitude a_q and (*b*) subharmonic–quarter-harmonic phase difference ϕ_q for intermittency between stable double pairing SDP and the quarter-harmonic chaotic attractor QCA for $St_D \approx 1.20$, $Re_D \approx 2.3 \times 10^4$, $x/D = 2.0$, at ▲, $a_f \approx 1.26\%$; □, $a_f \approx 1.44\%$ and ●, $a_f \approx 1.65\%$.

$a_f \approx 1.65\%$ (almost all SDP). For cases (ii) and (iii), the p.d.f. is clearly bimodal, demarcated by a local minimum at $a_q \approx 0.09$. For case (i), there is no second peak above $a_q \approx 0.09$, consistent with the observation that the signal is virtually all QCA. PDFs of ϕ_q for the same three cases reveal a large peak in the range $0.3 \leqslant \phi_q \leqslant 0.43$ for case (iii), with the peak becoming less distinct and shifting to lower ϕ_q as the SDP fraction decreases (figure 18*b*). This causes a problem in using ϕ_q thresholds to discriminate SDP from QCA, since the threshold ranges might be different from each a_f. For three cases at high a_f (where the ϕ_q peak is quite distinct and ϕ_q thresholds can be selected by inspection), the distributions of periodic segment lengths were compared using joint $a_q - \phi_q$ thresholds and a_q thresholds alone and found to be similar. Thus, the discrimination between SDP and QCA was done based on the amplitude threshold $a_q = 0.09$. Another threshold is the minimum periodic segment length τ_{min} (measured in quarter-harmonic periods). We found that statistics were similar for $2 \leqslant \tau_{min} \leqslant 5$, which were distinctly different from statistics for $\tau_{min} = 1$; thus, scaling exponents were averaged over the threshold range $2 \leqslant \tau_{min} \leqslant 5$. There were variations of q with different data sets, thresholds, and numbers of bins in the p.d.f.s, with deviations as

much as 20% from the mean value. Even with these variations, the statistics most closely support type-II intermittency.

REFERENCES

AUBRY, N., HOLMES, P., LUMLEY, J. L. & STONE, E. 1988 The dynamics of coherent structures in the wall region of a turbulent boundary layer. *J. Fluid Mech.* **192**, 115.

BERGÉ, P., DUBOIS, M., MANNEVILLE, P. & POMEAU, Y. 1980 Intermittency in Rayleigh–Bénard Convection. *J. Phys. (Paris) Lett.* **41**, L-344.

BERGER, W. D. 1993 Visualization of some vortex interactions in a circular jet. BS senior thesis, University of Houston Mechanical Engineering Dept.

BRANDSTÄTER, A. & SWINNEY, H. L. 1987 A strange attractor in weakly turbulent Couette–Taylor flow. *Phys. Rev.* A **35**, 2207.

BRIDGES, J. E. 1990 Application of coherent structure and vortex sound theories to jet noise. PhD dissertation, University of Houston Mechanical Engineering Department.

BRIDGES, J. E. & HUSSAIN, F. 1992 Direct evaluation of aeroacoustic theory in a jet. *J. Fluid Mech.* **240**, 469.

BROWAND, F. K. & LAUFER, J. 1975 Roles of large scale structures in the initial development of circular jets. In *Turbulence in Liquids* (ed. J. L. Zakin, G. K. Patterson), p. 333. University of Missouri-Rolla.

BROZE, G. & HUSSAIN, F. 1991 Spatiotemporal dynamics in transitional jet flows. In *Nonlinear Dynamics of Structures* (ed. R. Sagdeev, U. Frisch, F. Hussain, S. S. Moiseev & N. S. Grokhin), pp. 391–417. World Scientific.

BROZE, G. & HUSSAIN, F. 1994 Nonlinear dynamics of forced transitional jets: periodic and chaotic attractors. *J. Fluid Mech.* **263**, 93 (referred to herein as BH).

COHEN, J. & WYGNANSKI, I. 1987 The evolution of instabilities in the axisymmetric jet. Part 2. The flow resulting from the interaction between two waves. *J. Fluid Mech.* **176**, 191.

COULLET, P. & TRESSER, J. 1978 Iterations d'endomorphismes et groupe de renormalisation. *J. Phys. (Paris)* **C5**, 25.

CROSS, M. & HOHENBERG, P. C. 1993 Pattern formation outside of equilibrium. *Rev. Mod. Phys.* **65**, 851.

CROW, S. C. & CHAMPAGNE, F. H. 1971 Orderly structure in jet turbulence. *J. Fluid Mech.* **48**, 567.

DRAZIN, P. G. & REID, W. H. 1985 *Hydrodynamic Stability.* Cambridge University Press.

DUBOIS, M., RUBIO, M. A. & BERGÉ, P. 1983 Experimental evidence of intermittencies associated with a subharmonic bifurcation. *Phys. Rev. Lett.* **51**, 1446.

FEIGENBAUM, M. J. 1978 Quantitative universality for a class of nonlinear transformations. *J. Statist. Phys.* **19**, 25.

GERSTEN, K., KISKE, S., PAGENDARM, H.-G., SCHMITZ, O. & SCHMUCKER, A. 1985 Vortex breakdown control by jet injection. *Proc. Colloquium on Vortex Breakdown, Feb. 11–12, RWTH Aachen*, pp. 101–118.

GOLUBITSKY, M. & SCHAEFFER, D. G. 1985 *Singularities and Groups in Bifurcation Theory*, vol. 1. Springer.

GROSSMANN, S. & THOMAE, S. 1977 Invariant distributions and stationary correlation functions of one-dimensional discrete processes. *Z. Naturforsch.* **32A**, 1353.

GUCKENHEIMER, J. & HOLMES, P. 1983 *Nonlinear Oscillations, Dynamical Systems and Bifurcations of Vector Fields.* Springer. (Corrected second printing, 1986).

HOHENBERG, P. C. & SHRAIMAN, B. I. 1989 Chaotic behavior of an extended system. *Physica* D **37**, 109.

HUSAIN, H. S. & HUSSAIN, A. K. M. F. 1989 Subharmonic resonance in a shear layer. In *Advances in Turbulence 2* (ed. H. H. Fernholz & H. E. Fiedler), pp. 96–101. Springer.

HUSAIN, H. S. & HUSSAIN, F. 1995 Experiments on subharmonic resonance in a shear layer. *J. Fluid Mech.* **304**, 343–372.

HUSSAIN, A. K. M. F. & ZAMAN, K. M. B. Q. 1978 The free shear layer tone phenomenon and probe interference. *J. Fluid Mech.* **87**, 349.

HUSSAIN, A. K. M. F. & ZAMAN, K. M. B. Q. 1981 The 'preferred mode' of the axisymmetric jet. *J. Fluid Mech.* **110**, 39.

JENSEN, M. H., KADANOFF, L. P., LIBCHABER, A., PROCACCIA, I. & STAVANS, J. 1985 Global universality at the onset of chaos: results of a forced Rayleigh–Bénard experiment. *Phys. Rev. Lett.* **55**, 2798.

KAMBE, T. 1969 The stability of an axisymmetric jet with parabolic profile. *J. Phys. Soc. Japan* **26**, 566.

LESSEN, M. & SINGH, P. J. 1973 The stability of axisymmetric free shear layers. *J. Fluid Mech.* **60**, 443.

LIBCHABER, A. & MAURER, J. 1980 Une experience de Rayleigh–Bénard de geometrie reduite; multiplication, accrochage et demultiplication de fréquences. *J. Phys. (Paris) Lett.* **41**, C–C51.

MICHALKE, A. 1971 Instabilität eines kompressiblen runden Freistahls unter Berücksichtigung des Einflusses der Strahlgrenzschichtdicke. *Z. Flugwiss.* **9**, 319.

MIKSAD, R. W., JONES, F. L. & POWERS, E. J. 1983 Measurements of nonlinear interactions during natural transition of a symmetric wake. *Phys. Fluids* **26**, 402.

MOLLENDORF, J. C. & GEBHART, B. 1973 An experimental and numerical study of the viscous instability of a round laminar jet with and without thermal buoyancy for symmetric and asymmetric disturbances. *J. Fluid Mech.* **61**, 367.

MONKEWITZ, P. A. 1988 Subharmonic resonance, pairing and shredding in the mixing layer. *J. Fluid Mech.* **188**, 223.

MORRIS, P. J. 1976 The spatial viscous instability of axisymmetric jets. *J. Fluid Mech.* **77**, 511.

MULLIN, T. & PRICE, T. J. 1989 An experimental observation of chaos arising from the interaction of steady and time-dependent flows. *Nature* **340**, 294.

MUYLAERT, I. M. 1980 Effect of compressibility on vortex bursting on slender delta wings. *VKI Project Rep.* 1980–21.

NEWHOUSE, S., RUELLE, D. & TAKENS, F. 1978 Occurrence of strange axiom-A attractors near quasiperiodic flow on T^m, $m \leqslant 3$. *Commun. Math. Phys.* **64**, 35.

NOACK, B. R., OHLE, F. & ECKELMANN, H. 1992 Construction and analysis of differential equations from experimental time series of oscillatory systems. *Physica* D **56**, 389.

POMEAU, Y. & MANNEVILLE, P. 1980 Intermittent transition to turbulence in dissipative dynamical systems. *Commun. Math. Phys.* **74**, 189.

RINGUET, E., ROZÉ, C. & GOUESBET, G. 1993 Experimental observation of type-II intermittency in a hydrodynamic system. *Phys. Rev.* E **47**, 1405.

RITZ, CH. P. & POWERS, E. J. 1986 Estimation of nonlinear transfer functions for fully developed turbulence. *Physica* D **20**, 320.

RUELLE, D. & TAKENS, F. 1971 On the nature of turbulence. *Commun. Math. Phys.* **20**, 167.

SCHUSTER, H. G. 1988 *Deterministic Chaos.* New York: VCH.

SHTERN, V. N. & HUSSAIN, F. 1993 Hysteresis in a swirling jet as a model tornado. *Phys. Fluids* A **5**, 2183.

SPOTAR, S. YU. & TEREKHOV, V. I. 1987 Two spontaneously alternating regimes of a vortex flow above a plane. *J. Appl. Mech. Tech. Phys.* **N2**, 68–70.

SREENIVASAN, K. R. 1985 Transition and turbulence in fluid flows and low-dimensional chaos. In *Fundamental of fluid mechanics* (ed. S. H. Davis & J. L. Lumley), pp. 41–67. Springer.

VAN ATTA, C. W. & GHARIB, M. 1987 Ordered and chaotic vortex streets behind circular cylinders at low Reynolds numbers. *J. Fluid Mech.* **174**, 113.

WILLIAMS-STUBER, K. & GHARIB, M. 1990 Transition from order to chaos in the wake of an airfoil. *J. Fluid Mech.* **213**, 29.

ZAMAN, K. M. B. Q. & HUSSAIN, A. K. M. F. 1980 Vortex pairing in a circular jet under controlled excitation. Part 1. General jet response. *J. Fluid Mech.* **101**, 449.